CENTRO DE INVESTIGACIONES
EN OPTICA, A.C.

"DIFFRACTION BEHAVIOUR DUE TO A PHASE STEP IN DIFFERENT BEAMS AND ANALYSIS IN GLUCOSE MEASUREMENT"

Thesis submitted in fulfillment of the requirements for the Ph.D. degree in science (Optics)

Presents: Luis Miguel González Ortíz

Advisor: Dr. Moisés Cywiak Garbarcewicz

"Final version. Includes changes suggested by reviewers"

León · Guanajuato · México
December 2024

Seek the Lord while he may be found; call on him while he is near

ISAIAH 55:6

Thank you, God, for sustaining me in moments of uncertainty.

Dedications

"This work is dedicated to my wife Etna and my son Neizan, whose understanding and support have enabled me to complete it."

Acknowledgments

I want to my family for their constant love and guidance throughout this journey.

I am deeply grateful to my advisor, Professor Dr. Cywiak, whose steadfast and unwavering commitment to the project was crucial to its success. I would also like to thank Dr. Cervantes, Dr. Moreno, Dr. Flores and Dr. Padilla for their valuable feedback and recommendations. My sincere thanks go to the CIO staff for their assistance in providing the essential resources needed for this project.

I am grateful to CONACYT for their financial support.

Abstract

This thesis explores the optical diffractometry of Fresnel diffraction from transmission phase steps when illuminated by sources with varying spatial profiles. The study aims to deepen the understanding of how different spatial light distributions interact with abrupt phase changes in an optical medium, resulting in distinctive diffraction patterns.

Fresnel diffraction from phase steps has been extensively studied, but this research investigates the effects of different illuminating source profiles on the resulting diffraction patterns in transmission mode. The goal is to extend this method's applicability to clinical purposes, where precision is crucial.

The experimental setup involves creating phase steps in a transparent medium and illuminating them with sources of distinct spatial profiles. The resulting diffraction patterns are measured to understand how variations in the spatial distribution of light influence interference and diffraction. The Fresnel Gaussian Shape Invariant (FGSI) method is employed to precisely calculate coherent light propagation through optical setups containing phase steps. This method uses a superposition of Gaussian wavelets, capturing essential field characteristics, and simplifies programming while yielding accurate results for short propagation distances and various illumination sources, including non-diffracting beams.

The research includes calculations with different spatial profiles, such as Gaussian beams, Bessel beams, and non-diffracting Airy beams. Analyzing these profiles aims to establish general sensitivity formulas in the paraxial region, which are vital for optical applications. The non-diffracting Airy beam, in particular, is highlighted for its potential in clinical and metrological applications due to its ability to maintain its shape over long distances.

The study not only provides theoretical and numerical analysis but also validates these findings through rigorous experiments, ensuring the reliability and accuracy of the results. This comprehensive analysis contributes to a deeper understanding of optical diffractometry, enhancing precision in metrology and opening new possibilities in clinical applications.

List of Figures

Figure 2. 1. Representation of the phase step in reflection mode. 4
Figure 2. 2. Normalized intensity for a phase step in one-dimensional reflection mode based on Figure 2.1 6
Figure 2. 3. Geometrical representation of the phase step in transmission mode. 7
Figure 2. 4. Representation of a phase step in transmission mode. 8
Figure 2. 5. Normalized intensity due to the phase step that is presented in the studied case. 10
Figure 2. 6. Diffracted light in a phase plate with a small angle. 11
Figure 2. 7. Fresnel diffraction from an arbitrary aperture. 14
Figure 2. 8. Experimental setup for Fresnel diffraction from a variable circular step. 16
Figure 2. 9. Calculated visibility of diffraction fringes from a 1D step. 17
Figure 2. 10. Fresnel diffraction from a phase plate to determine the EFL. 19
Figure 2. 11. Sketch of the experimental setup. 27
Figure 2. 12. Sketch of the experimental setup for measuring phase shifts in optical fibers. 29
Figure 2. 13. The experimental setup of quantitative phase imaging using scanning diffractometry. 32
Figure 2. 14. Geometry used to calculate the optical Fresnel diffraction of cylindrical and spherical waves from a phase plate. 34
Figure 3. 1. Plane wave illuminating a transparent plate. 36
Figure 3. 2. Normalized intensity profiles due to the Fresnel diffraction from the transmission phase step. ... 38
Figure 3. 3. Setup used in reference [34] as described in the text. 40
Figure 3. 4. Normalized intensity profiles obtained with FGSI for the setup of Figure 2.4. 41
Figure 3. 5. Comparison of the Gaussian beam obtained with the CCD and a simulated beam. 43
Figure 3. 6. Measurements of the diffraction due to a phase step. 44
Figure 3. 7. Experimental and theoretical normalized intensity profiles at the observation plane. 44
Figure 3. 8. Wavelets propagating through the low optical quality thin plate (LOQTP). 46
Figure 3. 9. Gray level contours of the normalized intensity distribution of a Hermite–Gauss (1, 0) mode beam obtained as described in the text, recorded by the CCD. 47
Figure 3. 10. Normalized intensity profile, at a plane of observation, of a cut along $y = 0$ *of Figure 3.9.* 48
Figure 3. 11. $HG_{1,0}$ *beam obtained to illuminate the phase step (PS).* 49
Figure 3. 12. Experimental and theoretical normalized intensity profiles at the observation plane for the illuminating obtained $HG_{1,0}$ *beam.* 50
Figure 4. 1. Normalized intensity profiles for an illuminating Gaussian beam at different glucose concentrations and different sensitivity values. 53
Figure 4. 2. Normalized intensity profiles calculated with FGSI. 56
Figure 4. 3. Fresnel diffraction from a transmission phase step surrounded by pure distilled water and illuminated by a Gaussian beam. 62
Figure 4. 4. Normalized intensity profiles due to the illuminating $HG_{1,0}$ *beam.* 63
Figure 4. 5. Normalized intensity profiles of an illuminating $HG_{3,0}$ *beam.* 63
Figure 4. 6. Normalized intensity profiles due to the illuminating Airy beam. 64
Figure 4. 7. Normalized intensity profiles for four hypothetical thicknesses of 1.0 mm + 0.0, 100.0, 200.0, and 300.0 nm. 67

Figure A. 1 Illustration of a Gaussian wavelet propagating from an initial up to an observation plane by iterative propagations. 72

List of Abbreviations

Abbreviation	Meaning
FGSI	Fresnel Gaussian Shape Invariant
CCD	Charge-Coupled Device
OBJ	Moving Object
BE	Beam Expander
BS	Beam Splitter
STEP	Phase Step
M	Mirror
EFL	Effective Focal Length
HF	Hydrofluoric Acid
LED	Light-Emitting Diode
HeNe	Helium-Neon
FWHM	Full-Width Half-Maximum
1D	One-dimension
OPD	Optical Path Difference
TPS	Transparent Phase Step
FD	Fresnel Diffraction
RWC	Radius of Wavefront Curvature
CMOS	Complementary Metal Oxide Semiconductor Sensor
LOQTP	Low Optical Quality Thin Plate

Nomenclature

Symbol	Description
S	Source.
S'	Virtual image source.
M_1	Left mirror.
M_2	Right mirror.
r_1	Distance of the reflected amplitude due to the left reflecting surface M_1.
r_2	Distance of the reflected amplitude due to the right reflecting surface M_2.
R	Distance from the source to the step plane.
R'	Distance from the step plane to a point on the screen.
P	Arbitrary point on the screen.
λ	Wavelength.
φ	Phase difference.
h	Height of the step, thickness of the plate.
n	Refractive index of the medium.
$U_1(P)$	Wave amplitude of the diffracted light.
U_0	Amplitude of incident wave.
C_0 , S_0	Fresnel integral representing the cosine and sine components.
$U_1^*(P)$	Complex conjugate of $U_1(P)$.
I_1	Normalized intensity for one dimensional phase step in reflection mode.
V	Visibility.
$I_{L.\max}$	Intensity of the maximum peak on the left side.
$I_{R.\max}$	Intensity of the maximum peak on the right side.
$I_{C.\min}$	Intensity of the minimum central peak.
Δ	Optical path difference in transmission mode.
N	Refractive index of the plate.
N'	Refractive index of the surrounding medium.
θ	Angle of incidence.
y	Distance in y-direction.
α	Small angle in a transparent wedge.
ρ	Periods of the fringes.
Ω	Spatial plane.
Σ	Spatial plane.
z_0	Distance from the source to the Ω plane.

z	Distance from Ω plane to the Σ plane. Distance from the focal point to the observation plane.
A	Aperture.
D	Aperture size.
$P(x, y)$	Point on the plane Σ.
$E(P)$	Optical disturbance.
A_s	Amplitude of the incident spherical wave.
θ_0	Angle between the vector OS and the positive direction of z.
k	Wave number.
$r0$	Distance from the origin to the source.
r	Distance from the origin to the observation point on Σ.
$U(P)$	Geometric field.
$\alpha(P)$	Modification of the geometric field by diffraction.
$\cos(\theta_0)$	Tilt factor.
a_c	Radius of the circular aperture.
m_s	Experimental slope.
V_2	Measured visibility with the incidence angle θ_2.
V_1	Measured visibility with the incidence angle θ_1.
f	Effective focal length (EFL).
θ_{Max}	Angle related to the EFL.
a	Aperture diameter placed before a positive lens.
d	Diameter of the observation spot.
x	Distance from the optical axis to the edge of the plate in the observation plane.
ΔT	Average period in the visibility of the diffraction fringes.
Δh	Height variation depending on refractive indices.
$\Delta h / \Delta T$	Etching rate.
λ_0	Wavelength of the source.
σ_G	Gaussian width.
σ_L	Lorentzian width.
PP_0	Arbitrary point on a screen perpendicular to the reflected ray.
$J_s(\xi_{01}, \xi_{02})$	Intensity emitted by an incoherent source.
$\upsilon_s(\xi_0)$, $\upsilon_s^*(\xi_0)$	Amplitude of the source and its conjugate.
κ	Constant.
δ	Dirac delta function.
$\otimes$	One-dimensional convolution.
$A(x_0)$	Diffracted amplitude of the coherent wave.

$I_{co}(x_0)$	Intensity of the coherent light, is the square of the absolute value of $A(x_0)$.
$S_t(x')$	Phase step function.
$I_s(\xi)$	Intensity distribution of an incoherent source.
I_0	Maximum intensity.
σ	Distribution width.
$I_n(x_0)$	Intensity of the partially coherent light.
β	Parameter which describes the width of the incoherent source.
l_c	Transverse coherence length.
I_{N_j}	Normalized intensity of the diffraction fringes.
Δy	Minimum distance from the plate's edge
d_{co}	Core fiber's diameter.
α'	Intersection angle between the fiber and the plate's edge.
n_m	Refractive index of the surrounding medium in experiment with transparent phase step.
n_{TPS}	Refractive index of the material of the TPS.
η	Extrema position parameter.
$x_{L\min}$	Position of the minima left fringe.
$x_{R\max}$	Position of the maxima right fringe.
$x_{C\min}$	Position of the minima central fringe.
$\Psi(s)$	Wavefront propagated with the Fresnel integral.
L_P	Width of a thin transparent plate.
n_0	Refractive index of air.
n_1	Refractive index of the solution under measurement.
n_2	Refractive index of the thin transparent plate.
x_F	Coordinate at the observation plane.
$\psi_F(x_F)$	Amplitude distribution at the plane of observation.
$C(z)$, $S(z)$	Fresnel cosine and sine functions.
i	Imaginary number.
$F(z)$	Complex distribution.
L_C	Container width.
D_A	Distance from the initial plane to the front container's surface.
D_B	Distance from the back container's surface to the observation plane.
D_0	Short distance from L0PQT to the initial plane.
r_0	Semi-width of the beam.
C	Concentration.

$HG_{1,0}$	Hermite-Gaussian (1,0).
C_1	Constant.
H_1	First-order Hermite polynomial.
$HG_{3,0}$	Hermite-Gaussian (3,0).
C_3	Constant.
H_3	Third-order Hermite polynomial.
S_e	Sensitivity of the system.
Ai	Airy Function

Table of contents

1. Introduction 1
2. Background research 3
2.1 Phase Step 3
2.2 Measuring the Refractive Index in Transparent Liquids 8
2.3 Determination of the Refractive Index Using a Transparent Wedge and Fresnel Fringes. . 11
2.4 Precise Measurement of Refractive Index and Light Wavelength. 12
2.5 High-Resolution Measurement of Thermal and Electromechanical Expansions Using Fresnel Diffraction 13
2.6 Precision Measurement of Thin Film Thickness 16
2.7 Focal length measurement based on Fresnel diffraction from a phase plate 19
2.8 Fabrication and characterization of glass 20
2.9 Analyzing Thin Film Phase Steps Using Diffraction Patterns and Spectral Profile. 21
2.10 Measuring source width and transverse coherence length 24
2.11 Measuring Phase Shifts in Optical Fibers 28
2.12 Quantitative Phase Imaging Using Scanning Diffractometry 30
2.13 Fresnel Diffraction of Cylindrical Wavefronts at Phase Plate Edges 33
3. Analytical description 35
3.1Diffraction of a phase step in transmission 35
3.2 Optical Setup for Measuring Glucose Concentration in Distilled Water Using FGSI: Analysis and Improvements 39
3.3 Experimental measurements 42
4. Numerical evaluation of the performance of the diffraction from a transmission phase step using FGSI 51
4.1 Normalized Sensitivity in Fresnel Diffraction Systems 51
4.2 Impact of system sensitivity for various beams 57
5. Conclusions 69
6. Annex. Wave-front propagation with FGSI 70
Bibliography 75

1. Introduction

The phenomenon of Fresnel diffraction from phase steps in both transmission and reflection modes, initially introduced in [1] and further analyzed in [2-5], is a relatively recent area of research. Investigations into this phenomenon have found numerous applications in metrology. This phenomenon occurs when a light wave encounters a sudden transition or an abrupt alteration in an optical medium, causing a sudden phase shift in the wave. This change can arise from variations in the refractive index of the material or the presence of a thin film within the medium.

When light encounters such an alteration, interference patterns are generated due to the phase discrepancies of the waves propagating through and around the phase step. This phenomenon has been studied in both transmission and reflection modes. The Fresnel-Kirchhoff integral is employed to calculate the diffraction associated with this phenomenon, whose fundamental equation involves several reflection amplitudes and parameters describing the interaction of light with the phase step, enabling accurate modeling and understanding of this optical behavior.

In reflection mode, the phenomenon is represented through the normalized intensity of a one-dimensional phase step. In transmission mode, it is crucial to consider the change in direction due to the refractive indices through which the beam passes. A transparent element with an abrupt change in thickness or refractive index creates a phase step in transmission. Examples of this include a transparent plate suspended in air or a transparent liquid, as well as a transparent film deposited on a part of a transparent substrate. When a wave passes through such a medium, its phase undergoes a sudden shift proportional to the optical path difference between two parallel rays passing through different sides of the step.

Practical applications of this phenomenon include the precise measurement of the refractive index in transparent liquids using the phase step technique, which leverages the known refractive index of a transparent plate to detect even small

changes in the surrounding medium's refractive index with an accuracy of up to five digits [6-9]. Additionally, nanometric displacement measurements with a resolution of 2 nm [10], thin film thickness measurements in nanometric and micrometric ranges [11-13], focal length measurements with 0.01% accuracy [14], and curvature radius calculations for cylindrical and spherical wavefronts [15] are possible. Other applications include real-time control of etching rates of transparent materials [16-17], determination of the central wavelength and linewidth of a light source [18], characterization of faint starlight [19], calibration of phase shifters [20], hologram reconstruction for obtaining quantitative 3D images of cells [21-22], and the study of linear and nonlinear temporal intensity patterns in single-mode optical fibers [23].

In this study, we conducted experiments on diffraction from a phase step in transmission. To analytically support our findings, it is necessary to calculate, in a closed-form expression, the complex amplitude distribution that occurs when a phase step diffracts an illuminating source. Generally, it is not possible to analytically calculate the integrals involved in propagating an illuminating source to an observation plane through an optical setup containing one or more phase steps. Therefore, an appropriate numerical method is required to provide accurate calculations within the Fresnel range. Among the numerical methods available for this task are sampling expansions [24], fractional Fourier transform [25], angular spectrum expansion [26], and ray tracing combined with Monte Carlo, based on Heisenberg's Uncertainty Principle [27].

In this report, we employed a numerical method called Fresnel Invariant Gaussian Beam (FGSI) [28-30]. This method represents the initial illuminating field by a superposition of Gaussian wavelets. Each wavelet begins at the initial plane and gathers three key characteristics of the local field as it travels to the observation plane: complex amplitude and linear and quadratic phases. One of the advantages of the FGSI method is its ability to iteratively propagate these wavelets through the optical setup, simplifying the programming process. Ultimately, the superposition of wavelets provides the overall propagation of the illuminating field. This method

has proven to be accurate in various types of optical setups, even for short propagation distances and, in principle, for all kinds of illumination, including non-diffracting beams [30]. Here, we benefit from these attributes to provide analytical support to our experimental results.

The numerical results obtained from studying the phase step must be validated through rigorous experimental procedures to ensure their accuracy and reliability. This validation is essential to confirm the theoretical predictions and numerical simulations presented in the studies. Recent approaches suggest that the diffracted wave generated at the discontinuity can be described using a modulated probability function, similar to methods used in quantum mechanics, to enrich the understanding of the physical interaction between the light beam and the phase step.

2. Background research

The work will begin with background research to learn about some of the applications that can be obtained by using Fresnel diffraction through a phase step. The theoretical approaches are presented in the thesis's annex.

2.1 Phase Step

The phase step phenomenon has gained attention as a focus of study due to its potential applications in metrology, as demonstrated by initial studies [1]. This phenomenon occurs when a light wave encounters a sudden transition or an abrupt alteration in an optical medium, causing a sudden change in the wave's phase. This change can arise from variations in the refractive index of the material or the presence of a thin film within the medium [2-5].

When light encounters this alteration, interference patterns are generated due to discrepancies in the phases of the waves propagating through and around the phase step; this phenomenon has been studied in both transmission and reflection modes.

The Fresnel-Kirchhoff integral is used to calculate the diffraction associated with this phenomenon. Equation (2.1) is fundamental for these calculations, where A represents the disturbance amplitude, r_1 is the distance of the reflected light amplitude from the left-reflecting surface M_1, and r_2 is the distance of the reflected amplitude from the reflecting right surface M_2, R is the distance from the light source to the step plane, R' is the distance from the step plane to a point on the screen. Figure 2.1 illustrates the parameters involved in this equation.

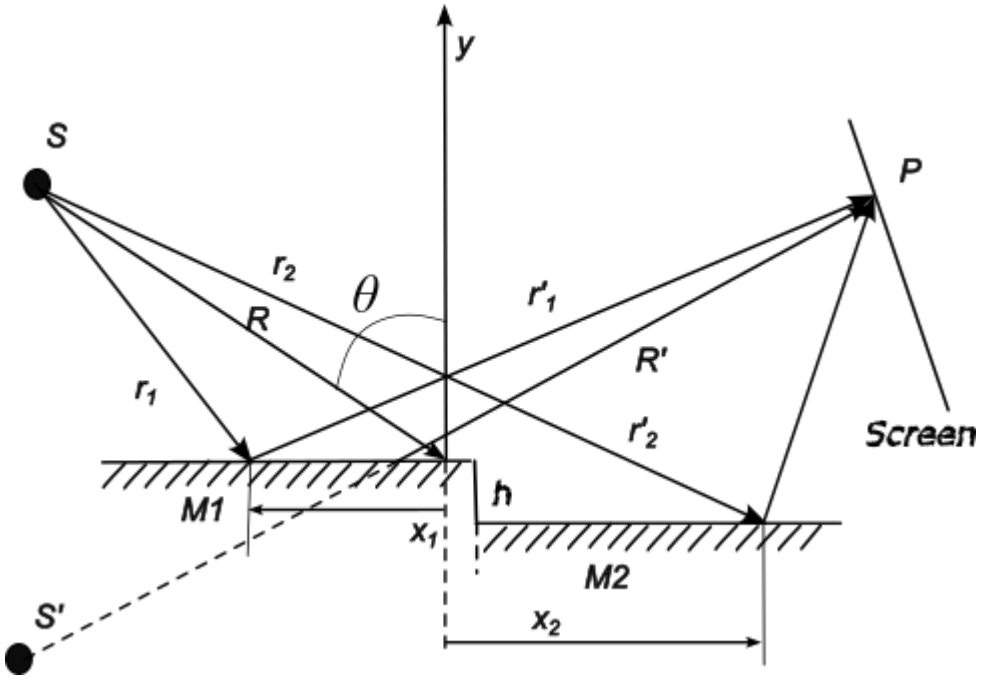

Figure 2. 1. Representation of the phase step in reflection mode. M1 and M2 are the reflecting surfaces, h is the height of the step, S represents the source of the cylindrical wave, S' is the virtual image of the source, and P is an arbitrary point on the screen. $\vec{r_1} = \vec{R} + \vec{x_1}$

$\vec{r_1}' = \vec{R}' - \vec{x_1}$, $\vec{r_2} = \vec{R} + \vec{x_2} + \vec{h}$, $\vec{r_2}' = \vec{R}' - \vec{x_2} - \vec{h}$.

In summary, the phase step phenomenon occurs when light interacts with an optical discontinuity, resulting in interference patterns that can be analyzed and utilized in various metrological applications. The Fresnel-Kirchhoff integral and the corresponding equation enable precise modeling and understanding of this optical behavior.

$$U_1(P) = \sqrt{\frac{-i}{\lambda}} A \left[r_1 \int_{-\infty}^{x_0} \frac{e^{ik\left(r_1 + r_1'\right)}}{\sqrt{r_1\, r_1'}}\, dx_1 \;+\; r_2 \int_{x_0}^{+\infty} \frac{e^{ik\left(r_2 + r_2'\right)}}{\sqrt{r_2\, r_2'}}\, dx_2 \right].$$

(2.1)

From Equation (2.1), by performing variable changes to define the, r_1, r_1', r_2 and r_2' in terms of R, R' and the coordinates x_1, x_2, considering the Fresnel approximation, and taking into account that the integral is even, Amiri et al. obtain the Equation (2.2) [1]

$$U_1(P) = \sqrt{\frac{-i}{2}} U_0 \left[\frac{1}{2}(1+i)\left(r_1 + r_2 e^{i\varphi}\right) + \left(C_0 + i\, S_0\right)\left(r_1 - r_2 e^{i\varphi}\right) \right] \qquad (2.2)$$

where U_0 is the amplitude of the incident wave, $\varphi = 4\pi h \cos\theta / \lambda$, and C_0, S_0 are the Fresnel integrals representing the cosine and sine components, respectively. To obtain the intensity, Amiri et al. multiplied the wave amplitude $U_1(P)$ by its complex conjugate $U_1^*(P)$, resulting in Equation (2.3).

$$\begin{aligned} I_1 = {} & I_0\, r_1\, r_2 \left[\frac{1}{2}\cos\varphi - \left(C_0 + S_0\right)\sin\varphi - \left(C_0^2 + S_0^2\right)\cos\varphi \right] \\ & + \frac{I_0}{2}\left[\left(\frac{1}{2} + C_0^2 + S_0^2 \right)\left(r_1^2 + r_2^2\right) + \left(C_0 + S_0\right)\left(r_1^2 - r_2^2\right) \right] \end{aligned} \qquad (2.3)$$

Figure 2.2 presents the normalized intensity result (Equation (2.3)) for a one-dimensional phase step in reflection mode. This represents a region where the phase of the incident wave undergoes an abrupt change. Such a phase change can occur, for example, when the wave encounters a surface with a discontinuity in refraction or geometry.

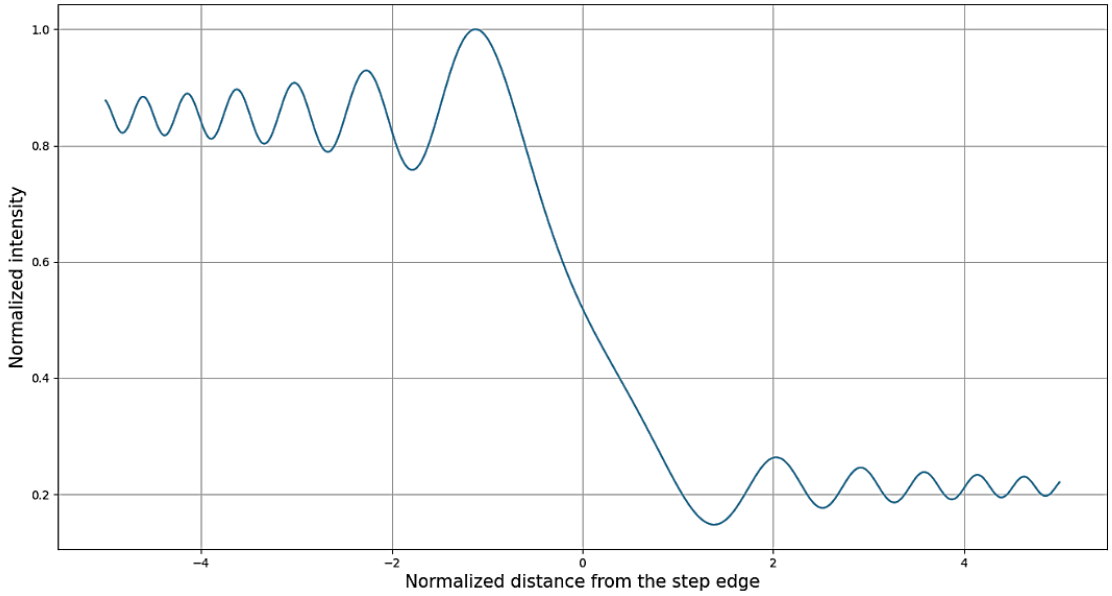

Figure 2. 2. Normalized intensity for a phase step in one-dimensional reflection mode based on Figure 2.1, $h = \lambda / 5$ *for a red beam,* $\theta = 29.15°$, $x_1 = -10.7$ *cm,* $x_2 = 15$ *cm.*

On the other hand, for the transmission mode, the beam's direction changes as it passes through materials with different refractive indices. A transparent element with an abrupt change in its thickness or refractive index creates a phase step in transmission. Examples include a transparent plate held in air or a transparent liquid, as well as a transparent film deposited on part of a transparent substrate. When a wave passes through such a medium, its phase undergoes a sudden change. The magnitude of this phase change is proportional to the optical path difference between two parallel rays traversing different sides of the step, $\Delta = (IMH) - (IM')$ as shown in Figure 2.3 [6]. Equation (2.4) can be used to determine the optical path difference by considering the refractive indices and the angle of incidence. In this

equation, N represents the refractive index of the plate with thickness h immersed in a medium with a refractive index n.

$$\Delta = h\left[\sqrt{N^2 - n^2 \sin^2 \theta_i} - n\cos\theta_i\right] \tag{2.4}$$

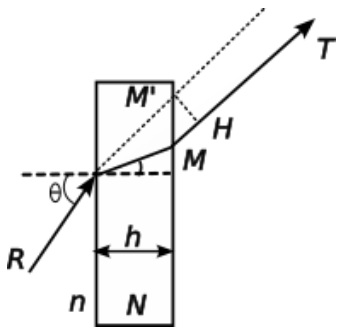

Figure 2. 3. Geometrical representation of the phase step in transmission mode, N is the step refractive index, h is the thickness of the step, n is the refractive index of the medium, and RT is the optical path of the ray.

In the reported studies, the visibility of the phenomenon is utilized and calculated as shown in the following Equation (2.5).

$$V = \frac{\frac{1}{2}\left(I_{L.\max} + I_{R.\max}\right) - I_{C.\min}}{\frac{1}{2}\left(I_{L.\max} + I_{R.\max}\right) + I_{C.\min}}. \tag{2.5}$$

Based on Figure 2.2, $I_{L.\max}$ is the intensity of the maximum peak on the left side, $I_{R.\max}$ is the intensity of the maximum peak on the right side, and $I_{C.\min}$ is the intensity minimum value of the central peak, which is better illustrated in Figure 2.5.

2.2 Measuring the Refractive Index in Transparent Liquids

The refractive index of liquids can be measured with high accuracy using the phase step technique. This method utilizes the known refractive index of a transparent plate. Even a small change in the refractive index of the surrounding medium where the plate is immersed can be detected at the observation plane through changes in intensity, or as discussed in the literature, through visibility as given by Equation (2.5).

In [7], the phase change in diffraction due to the phase step is utilized. A parallel-faced plate is placed at an angle θ. The upper half of the beam propagates to the observation plane without alteration, while the other half experiences a phase change due to the refractive index change of the parallel-faced plate. Figure 2.4 shows that at point P, the intensity is observed and calculated using the Fresnel integral.

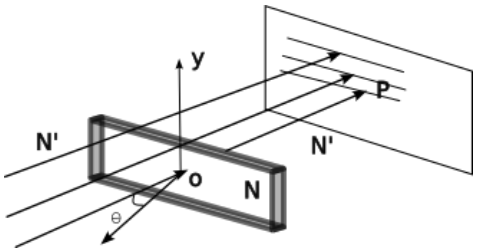

Figure 2. 4. Representation of a phase step in transmission mode.

The phase difference between the two beams, one passing through the plate and the other through the surrounding medium, results in a diffraction pattern at the observation plane. This phase difference is described by Equation (2.6),

$$\varphi = \frac{2\pi h}{\lambda} N'(\sqrt{N^2 - \sin^2\theta} - \cos\theta)\,. \tag{2.6}$$

where λ is the wavelength, h is the thickness of the plate, N is the refractive index of the plate, and N' is the refractive index of the surrounding medium.

Below are three methods to determine the refractive index of a transparent plate:

1. Fitting the Theoretical Curve to Experimental Data of Phase Change versus Angle of Incidence at Maximum Visibility:

- In this method, the refractive index is obtained by fitting Equation (2.6) to the experimental results of phase change versus the angle of incidence at maximum visibility. This involves identifying the angle of incidence where the visibility of the diffraction fringes is at its peak. Using these data points to fit Equation (2.6), the refractive index of the plate can be determined by comparing the experimental data with the adjusted theoretical curve.

2. Counting States with Maximum Visibility within an Angle of Incidence Range:

- This method involves counting the number of states with maximum visibility within a specific range of the angle of incidence, $\theta_1 - \theta_2$. The phase change data and corresponding angles of incidence, along with the plate thickness, are used in Equation (2.6) to solve for the refractive index. This approach relies on the relationship between maximum fringe visibility and the angles of incidence to determine the refractive index of the plate.

3. Counting States with Similar Visibility in Two Successive Angles of Incidence Ranges:

- In this method, the number of states with similar visibility in two successive angles of incidence ranges is counted. The visibility data are used to calculate the refractive index of the plate based on the changes in the angles of incidence. By comparing the states of visibility in adjacent intervals, the refractive index of the plate can be determined precisely.

Using these methods, the refractive index of a transparent liquid can be calculated when a transparent plate with a known refractive index is illuminated and installed in a rectangular cell containing the liquid. This equation is applied in the context of measuring the refractive index of a liquid using Equation (2.7). By applying this equation and performing calculations based on the experimental data of phase change and angles of incidence, the refractive index of the liquid can be determined accurately. Given the known refractive index of the plate, the refractive index of the transparent liquid is measured using Equation (2.7), adjusting for the refractive index of the liquid N'.

$$\varphi = \frac{2\pi h}{\lambda}\left(\sqrt{N^2 - \sin^2\theta} - \sqrt{N'^2 - \sin^2\theta} \right). \tag{2.7}$$

Figure 2.5 shows an example of the normalized intensity due to diffraction, obtained when a monochromatic light beam passes through a phase step in transmission mode, which is the case studied here.

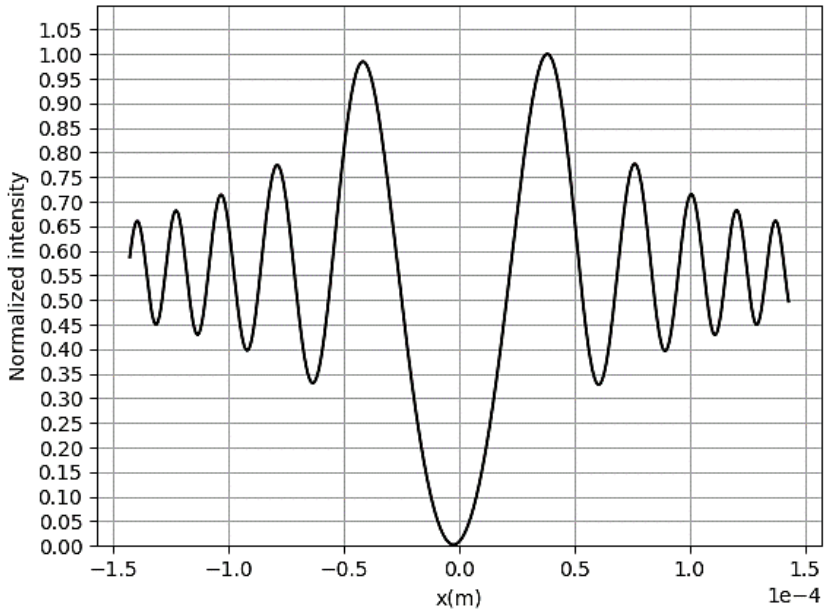

Figure 2. 5. Normalized intensity due to the phase step that is presented in the studied case.

2.3 Determination of the Refractive Index Using a Transparent Wedge and Fresnel Fringes.

In another variant of the study [8], it is demonstrated that by illuminating a transparent wedge with a small angle, a plate is obtained that imposes a phase varying linearly in y-direction. The thickness of the wedge at a distance y from the vertex is given by $y \tan \alpha$. Considering this in Equation (2.2) for normal illumination of the wedge, Tavassoly et. al (2.8) obtained the following expression,

$$\varphi = \frac{2\pi y}{\lambda}\left(N - N'\right)\tan\alpha \quad . \tag{2.8}$$

The vertex of the wedge is perpendicular to its surface, and when it is illuminated with a parallel monochromatic light beam, as shown in Figure 2.6, Fresnel fringes are formed on a screen positioned perpendicular to the direction of the beam propagation. These fringes are caused by the abrupt change in the refractive index at the lateral boundary of the wedge.

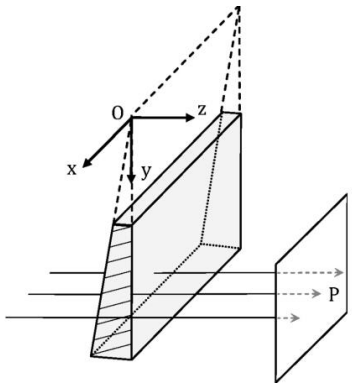

Figure 2. 6. Diffracted light in a phase plate with a small angle. The diffraction is due to changes in the optical path.

The visibility of the diffraction fringes varies periodically in the y-direction between zero and one, perpendicular to the vertex of the wedge. For a known or measured wedge angle, the refractive index of the wedge can be obtained by

measuring the period length using a CCD. To measure the refractive index of a transparent liquid or solution, the wedge is placed in a transparent rectangular cell containing the sample. The cell is then illuminated perpendicularly, and the visibility period is measured. The refractive index can be measured with a relative uncertainty level of 10^{-5} [8], by measuring the distance between two similar visibility states at the far ends and dividing this distance by the number of periods in between, yielding the period ρ. With N, the refractive index of air, they can find the refractive index we are looking for Equation (2.9)

$$N = N' + \frac{\lambda}{\rho \tan\alpha} \quad . \tag{2.9}$$

2.4 Precise Measurement of Refractive Index and Light Wavelength.

When a quasi-monochromatic parallel light beam illuminates the edge of a transparent parallel plate, diffraction fringes appear on a plane perpendicular to the transmitted beam's direction. This phenomenon arises due to the sudden phase change imposed by the abrupt refractive index transition at the plate's boundary, resulting in Fresnel diffraction patterns. The visibility of these fringes varies with the plate's thickness, refractive index, light wavelength, and angle of incidence.

This study [9], illustrates that by systematically recording the visibility versus angle of incidence, they can achieve precise measurements of the plate's refractive index, thickness, and wavelength of light used. Furthermore, our findings underscore the indispensable nature of this technique in characterizing color dispersion within plate-shaped samples. They apply this method to effectively measure dispersion in fused silica plates and determine refractive indices for soda-lime glass sheets.

This versatile technique offers high accuracy across a broad range of parallel plate thicknesses. Utilizing a plate of known thickness enables precise determination of the light wavelength. Notably, contrast variations in the fringes are observed particularly for thicker plates and at angles of incidence different from zero.

For $\varphi = (2m+1)\pi$ with m being an integer, the phase step's contribution causes equal contrast on both sides of the fringes. The visibility changes with variations in the angle of incident light, which induces phase shifts. Moreover, this visibility decreases with distance as the plate moves away from the light source.

The transmittances on either side of the plate edge are not equal, and the transmission coefficient of the plate varies significantly with changes in the angle of incidence, unlike the surrounding medium's transmission coefficient. To minimize these differences in coefficients, it is preferable to work with polarized light path angles of incidence close to the Brewster angle.

2.5 High-Resolution Measurement of Thermal and Electromechanical Expansions Using Fresnel Diffraction

The study introduces a technique utilizing a directed laser beam aimed at a two-dimensional circular phase step, as shown in Figure 2.7, the light from a point source strikes a plane Ω located at a distance z_0 from the source S, which contains an aperture A. The diffracted rays from various points on the aperture then interfere with another plane Σ at a distance z, creating the Fresnel diffraction pattern. To measure variations in visibility in Fresnel diffraction fringes by altering the step height with an external object. This technique is demonstrated by measuring thermal expansion in the radius of a tungsten wire and electromechanical expansion in a thin piezoelectric ceramic. The results show high resolution in the order of a few nanometers and good agreement with theory [10].

Compared to conventional interferometers, this method offers several advantages such as intrinsic calibration based on the wavelength of light and reduced sensitivity to mechanical vibrations and optical surface roughness. The device can measure displacements of several millimeters with a resolution in the nanometer range [10].

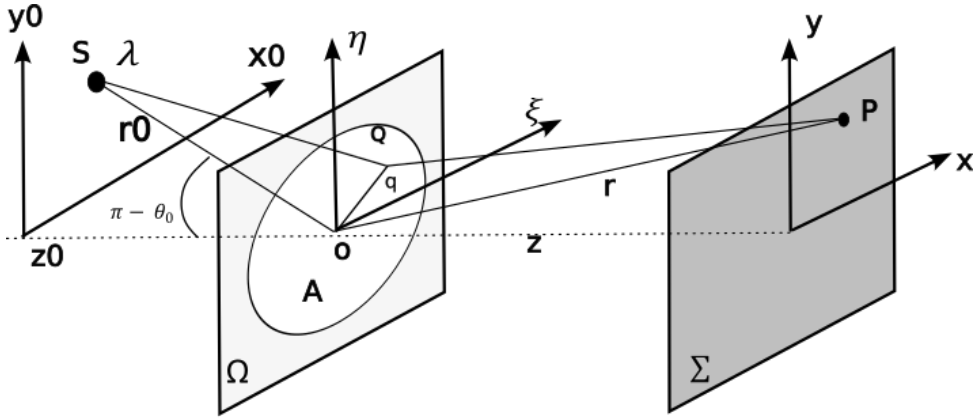

Figure 2. 7. Fresnel diffraction from an arbitrary aperture. Light from a point source S strikes a plane Ω located at a distance z_0 from the source, which contains an aperture A. The diffracted rays from various points on the aperture then interfere on another plane Σ at a distance z, creating the Fresnel diffraction pattern.

Coherent and nearly monochromatic light with wavelength λ originates from a point source S and reaches a mask Ω with an aperture of arbitrary shape A and size D. The origin of the coordinate system is established at point O on Ω. The optical disturbance at a point $P(x, y)$ on the plane Σ, which is parallel to and at a distance z from the mask Ω, is considered. The Fresnel-Kirchhoff approximation Equation (2.10), is used to analyze the paraxial region, where the distances between the source S or the point P and Ω are finite but large compared to D^2/λ.

$$E(P) = \frac{i}{\lambda} A_s \cos(\theta_0) \frac{e^{ik(r0+r)}}{r0\, r} \int_A e^{ik\Delta} d\xi d\eta$$

$$= -U(P)\alpha(P)\cos(\theta_0) \qquad . \qquad (2.10)$$

where $U(P) = A_s \left(e^{ik(r0+r)} \big/ r0\, r \right)$, and $\alpha(P) = (-i/\lambda) \int_A e^{ik\Delta} d\xi d\eta$

In Equation (2.10), A_s represents the amplitude of the incident spherical wave, θ_0 is the angle between the vector OS and the positive direction of z, k is the wave number, $r0$ and r are the distances from the origin point to the source point and observation point respectively, and Δ is the path difference.

As can be seen, from $E(P)$, the optical disturbance is divided into three parts: a geometric field $U(P)$, a modification of the geometric field by diffraction $\alpha(P)$, and a tilt factor $\cos(\theta_0)$ according to Lambert's law. In [10], detailed expressions for each of these parts are provided, specifically for a circular aperture of radius a_c in the paraxial approximation, and the Fraunhofer and geometric limits are established.

The experimental setup for measuring nanometric displacements of a moving object (OBJ) is shown in Figure 2.8 and consists of a He-Ne laser, a beam expander (BE), a beam splitter (BS), a circular phase step (STEP) with two concentric mirrors (M), and a CCD camera to capture diffraction patterns.

The central mirror of the phase step was calibrated to modify its height, causing changes in the diffraction pattern recorded by the CCD camera. Khorshad, Hassani, and Tavassoly made measurements to evaluate the sensitivity of the proposed technique. Electromechanical expansions in piezoelectric ceramics were used, and the method proved sensitive to average displacements as small as 2 nm produced by a single thin piezoelectric ceramic. Thermal expansions in a tungsten wire with a diameter of only 1.5 mm were measured in the second experiment, successfully detecting expansions of approximately 3.2 nm in the wire's radius [10].

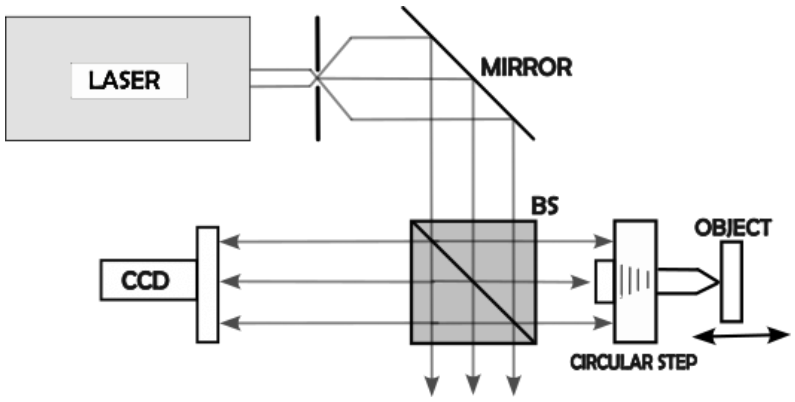

Figure 2. 8. Experimental setup for Fresnel diffraction from a variable circular step. It consists of the following components: BE, a beam expander; M, a mirror; BS, a beam splitter; STEP, a circular phase step; OBJ, a moving object; and a CCD camera.

2.6 Precision Measurement of Thin Film Thickness

In this method, a thin film prepared in the form of a step on a substrate and uniformly coated with a reflective material is illuminated by a coherent parallel beam of monochromatic light [11]. The visibility of these fringes depends on the film thickness, the angle of incidence, and the wavelength of the light. By measuring the visibility versus the angle of incidence, the film thickness can be determined with high precision, typically within a few nanometers [11]. The setup is based on Figure 2.1 to obtain the visibility of the diffraction fringes from the phase step in reflection mode. These fringes vary with θ and with the distance from the edge of the step h. The visibility is defined for the three central fringes as shown in Equation (2.4).

Figure 2.9 displays the visibility against the optical path difference divided by the wavelength $\Delta/\lambda = \varphi/2\pi$. The curve presented is universally applicable to any step with the same reflectance on both sides of the edge. This implies that by fitting experimental visibilities to this curve, it is possible to determine the step height or the film thickness. As the optical path difference changes by $\lambda/2$, which is equivalent to a change in film thickness by $\lambda/4$ in reflection, the visibility varies

from zero to one. By fitting the experimentally obtained visibilities, one can derive the step height or film thickness.

The straight lines that appear in the interval where the optical path difference divided by the wavelength is less than 0.25 or greater than 0.75 can be used to measure the film thickness. Since changing the angle of incidence allows for adjustment of the optical path difference in these regions, the plotted lines are useful for general film thickness measurements. In practice, visibilities are measured over an appropriate range of incidence angles, and the slope of the best-fit line is determined, which is then equated to the calculated slope using the following formula,

$$\tan\alpha = \frac{(V_2 - V_1)\lambda}{2h(\cos\theta_2 - \cos\theta_1)} \tag{2.11}$$

If $\Delta = 2h\cos\theta$ for the line corresponding to the left side of Figure 2.9.

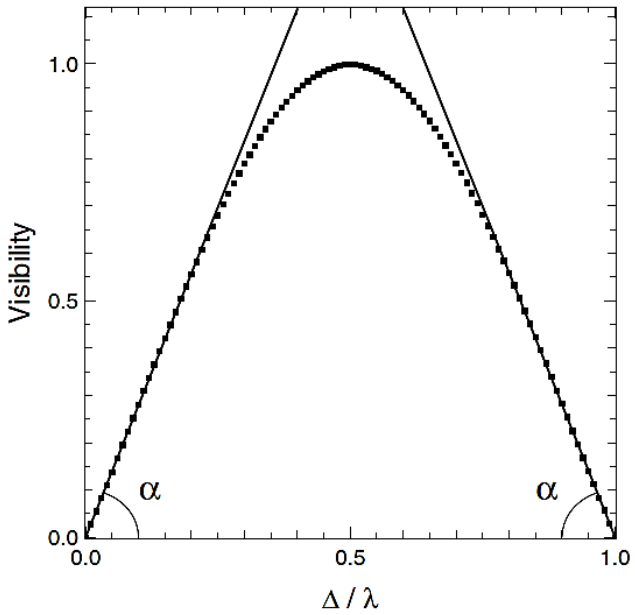

Figure 2. 9. Calculated visibility of diffraction fringes from a 1D step. The visibility is calculated with the three central diffraction fringes formed by the diffracted light from a 1D step and plotted against the optical path difference divided by the wavelength, Δ/λ.

The straight lines have inclination angles of 2.77 degrees with respect to the horizontal. By substituting $(V_2 - V_1)/(\cos\theta_2 - \cos\theta_1)$ from Equation (2.11) with the experimentally obtained slope m_s, the step height h is determined.

$$h = \frac{m_S \lambda}{5.54} \tag{2.12}$$

In the experimental procedure, a film is coated onto a partially masked glass slide using vacuum evaporation. The mask is then removed to create the required step in the film. Both sides of the step are coated with a reflective material, such as aluminum, to ensure uniform reflectance. The slide is mounted on a holder that can rotate horizontally and is illuminated with an expanded parallel laser beam. A CCD camera is mounted on an arm that can rotate around the axis of the holder and is connected to a computer via an image capture card.

The diameter of the laser beam used in the setup is 30 mm, and the angle of incidence can be varied with a precision of 1 arc minute. The CCD camera, positioned at a distance of 100 mm from the slide, records the diffraction pattern formed by the step when it is illuminated. By rotating the slide holder to change the angle of incidence, the CCD captures the diffraction pattern.

The authors illustrate three typical experimental diffraction patterns formed by steps and the corresponding intensity profiles averaged along lines parallel to the edge of the step.

2.7 Focal length measurement based on Fresnel diffraction from a phase plate

To measure the effective focal length (EFL) of optical imaging systems using Fresnel diffraction, a parallel monochromatic light beam is restricted by an aperture that makes it convergent through a positive lens system [14]. The beam illuminates the plate parallel to the observation plane, which may be positioned either before or after the focal point. In this case, z represents the distance from the focal point to the observation plane, as shown in Figure 2.10. The angle θ_{Max} is related to the EFL (f) and the aperture diameter by Equation (2.13).

$$\tan\theta_{Max} = \frac{a/2}{f} = \frac{d/2}{z} \tag{2.13}$$

where d is the diameter of the observation spot. The phase difference is expressed in terms of x, which is the distance from the optical axis to the edge of the plate in the observation plane, and $z = d/a$.

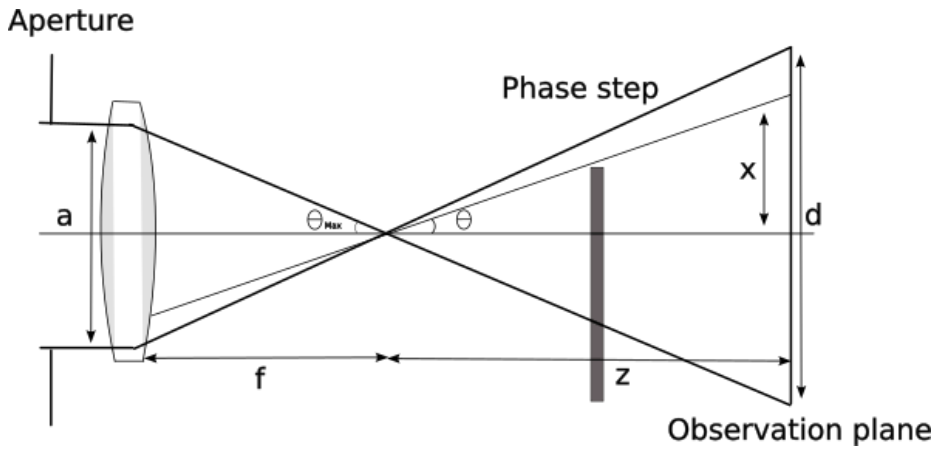

Figure 2. 10. Fresnel diffraction from a phase plate to determine the EFL.

This results in Equation (2.14) which represents the phase difference in terms of the parameters illustrated in Figure 2.10.

$$\varphi = \frac{2\pi h}{\lambda} N' \left[\sqrt{n^2 - \frac{x^2}{(zf)^2 + x^2}} - \sqrt{\frac{(zf)^2}{(zf)^2 + x^2}} \right] \tag{2.14}$$

This approach for accurately measuring effective focal lengths offers a straightforward method that avoids the need for complex elements while maintaining low levels of mechanical and optical noise compared to interferometric methods. The technique applies to a wide range of focal lengths, both positive and negative. Results obtained for five different lenses demonstrate significant consistency, validating the method's effectiveness and reliability, with accuracies reaching up to 0.02% [14].

2.8 Fabrication and characterization of glass

The study focuses on analyzing the effects of the concentration and temperature of the hydrofluoric acid (HF) solution on the etching rates of glass using wet etching. A novel method is employed, which involves a transparent plastic chamber filled with a diluted HF solution and a glass plate submerged in the solution, illuminated by a collimated laser beam. The resulting Fresnel diffraction pattern is recorded using a CCD camera, and the visibility of the diffraction fringes is calculated to assess the etching rate. The experimental setup used for this study is illustrated in Figure 2.1.

During the etching process, the continuous decrease in the thickness of the glass plate leads to periodic variations in the visibility of the diffraction fringes. It is observed that visibility is a periodic function of time, with an average period of $\Delta T = 450$ seconds. Additionally, a correlation is found between phase changes and variations in the glass plate thickness, allowing for the calculation of the etching rate. The phase change is given by 2π, as shown in Equation (2.6), and h varies with

$\Delta h = \lambda/(N-n)$, where the etching rate is $\Delta h/\Delta T$. When the refractive index of the glass plate is 1.5160 at λ = 633 nm and that of the solution is 1.3314, the etching rate when both sides of the glass are etched is 7.6 nm/s. As the concentration increases, the etching rate rises almost linearly. The effect of temperature on the etching rate is also investigated, using constant values for the refractive indices of glass and water at different temperatures. The experimental results show that, within the temperature range studied, changes in the etching rate are negligible [16].

2.9 Analyzing Thin Film Phase Steps Using Diffraction Patterns and Spectral Profile.

The phase step is examined in reflection mode, as illustrated in Figure 2.1. Based on this theory, the calculation of the Fresnel diffraction intensity for a phase step is conducted, highlighting how the spectral profile of light affects this pattern. It is observed that the visibility of the diffraction fringes decreases as the spectral width increases, as demonstrated by experimental data obtained from various light sources, including a Helium-Neon (HeNe) laser λ_0 = 632.899 nm and yellow λ_0 = 592 nm and green λ_0 = 513 nm Light Emitting Diodes (LEDs), all with a step size of h = 194 nm. A spectral line fitting approach is proposed to calculate the diffraction pattern and compare it with experimental data, allowing for the extraction of detailed information about the light spectrum used. This method is presented as a useful tool for analyzing the relationship between the spectral profile of light and its diffraction pattern in light source characterization applications.

The experimental setup was designed to study diffraction patterns using a one-dimensional coherent light source. In this setup, the light first passed through a narrow slit, which served to produce a collimated beam. This beam was then

directed at a sample with phase steps, which was mounted on a goniometer for precise angular adjustments.

Two distinct samples were prepared for the experiment, each featuring phase steps of different heights: h_1 = 200 nm and h_2 = 1000 nm. These samples were fabricated by depositing a thin layer of chromium onto flat glass substrates using an evaporation technique. The process ensured that the phase steps were accurately created with the desired heights $\lambda/4$.

For capturing the diffraction patterns, a stable He-Ne λ_0 = 632.899 nm laser was employed. The laser's monochromatic and coherent light provided a consistent and controlled illumination for the experiment. The diffraction patterns resulting from the interaction of the laser light with the phase steps on the samples were recorded and analyzed.

The intensity of the diffraction patterns was measured and compared with theoretical predictions. By fitting the experimental data to the intensity Equation (2.2), the heights of the phase steps h_1 and h_2 were accurately determined. This approach allowed for a precise assessment of the phase step heights based on the observed diffraction patterns.

For obtaining the experimental diffraction patterns, a stable HeNe laser was utilized. The laser's monochromatic and coherent light was directed onto the phase steps of the samples. The intensity of the resulting diffraction patterns was measured and compared with theoretical predictions using Equation (2.2). This approach allowed for the accurate determination of the phase step heights.

Subsequently, similar measurements were conducted by Hassani, Jabbari, and Tavassoly, using yellow and green LEDs. The yellow LED had a wavelength of λ_0 = 592 nm and a full-width at half-maximum spectral bandwidth of $FWHM$ = 19 nm, while the green LED had a wavelength of λ_0 = 513 nm and a spectral bandwidth of

$FWHM$ = 40 nm. These additional measurements provided data on how different light sources with varying spectral profiles affected the diffraction patterns, contributing to a comprehensive analysis of the phase steps and their impact on the resulting diffraction phenomena.

The diffraction patterns obtained were fitted to a Voigt spectral function to determine the central wavelength λ_0 and spectral width. In [18], a simplified Voigt function is defined by three parameters: the central wavelength λ_0, the Gaussian width σ_G, and the Lorentzian width σ_L. These parameters were estimated by fitting the Voigt function to the obtained experimental diffraction patterns, and were then used to calculate the full width at half maximum ($FWHM$) of the spectrum based on the fit results and the following relation:

$$FWHM = 0.5346 \times \sigma_L + \sqrt{0.2166 \times \sigma_L^2 + \sigma_G^2} \quad . \tag{2.15}$$

The results are summarized in Table 2.1, which shows the central wavelengths, spectral $FWHM$, and standard uncertainties after several measurements at different incidence angles. The accuracy of the measurements largely depends on the uniformity of the step heights along the edge of the step.

Spectral results for the green LED			Spectral results for the yellow LED	
Method	λ_0 (nm)	$FWHM$ (nm)	λ_0 (nm)	$FWHM$ (nm)
Spectrometer	513±3	40±1	592±3	19±1
Step 1	512±3	47.4±0.8	606±2	18.7±0.3
Step 2	507±22	46±1	594±9	15±4

Table 2.1

Additionally, a systematic discrepancy was observed between the results obtained from diffraction measurements and those from the commercial spectrometer readings. This discrepancy arose due to asymmetries in the spectral profiles of the LED sources used. Specifically, the spectral shapes of the LED sources exhibited irregularities or non-uniformities that affected the accuracy of the diffraction pattern analysis. These spectral distortions led to deviations in the measured central wavelengths and $FWHM$ values when compared to the results obtained using the spectrometer. The LEDs' non-ideal spectral characteristics thus introduced errors in the diffraction-based calculations, highlighting the impact of source quality and spectral purity on measurement precision.

2.10 Measuring source width and transverse coherence length.

In this study [19], Fresnel diffraction from a step in reflection mode is used to measure the source width and transverse coherence length. Both theoretical and experimental demonstrations show that these quantities can be determined by specifying the position of the minimum visibility in the diffraction pattern. To achieve this, a sodium vapor lamp with a variable slit in front of it is employed as a one-dimensional extended incoherent light source. Alipour and Tavassoly made measurements by recording a single diffraction pattern formed by the step.

Based on Figure 2.1, a quasi-monochromatic light beam originating from an incoherent one-dimensional extended source is considered. This beam reaches a cylindrical lens and then impinges upon a phase step of height h through another cylindrical lens with a focal length f . The objective is to calculate the intensity distribution of the light diffracted from the phase step to an arbitrary point P_0 on a screen that is perpendicular to the reflected ray.

The light emitted by the incoherent source has a mutual intensity given by Equation (2.16),

$$J_S(\xi_{01},\xi_{02}) := \left\langle \upsilon_S(\xi_0)\upsilon_S^*(\xi_0)\right\rangle = \kappa I_S(\xi_{01})\delta\left(\left|\xi_{01}-\xi_{02}\right|\right) \qquad (2.16)$$

where $\upsilon_s(\xi_0)$ and $I_s(\xi_0) = \left\langle \upsilon_s(\xi_0)\upsilon_s^*(\xi_0)\right\rangle$ are the complex amplitude and the intensity of the light from the source, respectively, κ is a constant, and δ is the Dirac delta function. The effect of propagation on the mutual intensity of an incoherent source can be described using the Van Cittert-Zernike theorem. For a cylindrical wave at a distance r_0 from the source, the amplitude can be expressed as $\upsilon_s/\sqrt{r_0}$.

The intensity of the partially coherent light diffracted from the step is obtained using the convolution theorem, resulting in the equation $I = \kappa J_i' \otimes I_{co}$, where $\otimes$ denotes the one-dimensional convolution. The intensity of the coherent light diffracted $I_{co}(x_0)$ is calculated through the Fourier transform of the amplitude of the diffracted coherent wave, as given by Equation (2.17).

$$A(x_0) = \frac{1}{\sqrt{\lambda R'}}\int_{-\infty}^{\infty} S_t(x')e^{i\pi x'^2/\lambda R'}e^{-i2\pi x_0 x'/\lambda R'}dx' \qquad (2.17)$$

where $S_t(x')$ is the function of the phase step and R' is a distance related to the reflected light (see Figure 2.1). The intensity $I_{co}(x_0)$ is the square of the absolute value of this amplitude $A(x_0)$.

The quasi-monochromatic light beam, emitted by a finite-width incoherent source, illuminates a 1D phase step through a cylindrical lens, producing a diffraction pattern on a screen. This setup allows for the study of how the visibility of the diffraction fringes varies with the width of the source, providing insights into the transverse coherence of the light.

The width of the light source affects the visibility of the diffraction patterns generated by a phase step. The intensity distribution of an incoherent source is modeled by a Gaussian function $I_s(\xi) = I_0 e^{-\xi^2/2\sigma^2}$, where I_0 is the maximum intensity and σ is the width of the distribution. The intensity of the partially coherent diffracted light $I_n(x_0)$ is obtained by convolving the intensity of the coherently diffracted light $I_{co}(x_0)$ with the intensity distribution of the source $I_s(\xi)$, resulting in Equation (2.18).

$$I_n(x_0) = \int_{-\beta}^{\beta} I_{co}(x_0 - \xi) I_s(\xi) d\xi \tag{2.18}$$

with $\beta = R'a/2f$ and a as the width of the source, the derivative of the normalized intensity with respect to x_0 is expressed as $\frac{dI_n(x_0)}{dx_0} = I_{co}(x_0 + \beta) - I_{co}(x_0 - \beta)$, which is used to determine the visibility of the diffraction fringes. The visibility decreases as the width of the source increases. The transverse coherence length l_c, a measure of the distance over which the light maintains a coherent phase, is related to the visibility function (Equation (2.4)) of the diffracted light: $l_c = \lambda R'/\pi\beta$, where λ is the wavelength of the light and β is the parameter describing the width of the incoherent source. As the width of the source increases, the visibility decreases, indicating lower transverse coherence because a wider source introduces more phase variations, reducing the ability for constructive and destructive interference.

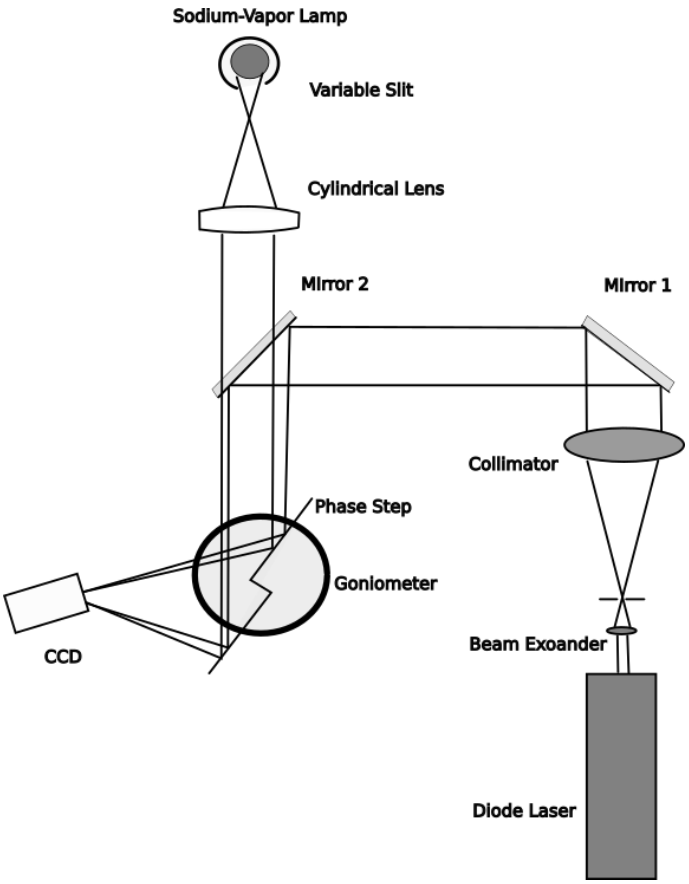

Figure 2. 11. Sketch of the experimental setup. A 670 nm diode laser beam illuminates a 690 nm high phase step at a 76° angle via two perpendicular mirrors. The diffraction pattern is captured by a CCD camera 213 mm from the step and sent to a PC.

The experimental system consists of a He-Ne laser with a wavelength λ = 632.8 nm used as a quasi-monochromatic light source. A 670 nm diode laser beam illuminates a 690 nm high phase step at a 76° angle via two perpendicular mirrors. The diffraction pattern is captured by a CCD camera 213 mm from the step and sent to a PC, as shown in Figure 2.11. The laser light passes through an adjustable slit, which acts as the one-dimensional incoherent source. The slit width can be varied to change the effective width of the source. The light then passes through a cylindrical lens with a focal length f = 200 mm, focusing the beam onto a phase step of height h. The phase step is fabricated on a glass plate with an adjustable height, introducing a phase difference between the two halves of the incident light beam.

The intensity distribution of the diffracted light is measured on a screen placed at a distance R' behind the phase step.

A CCD camera is used to measure the intensity by recording the intensity distribution on the screen. The captured images are analyzed using software to obtain normalized intensity profiles. Measurements are taken for different slit widths, varying from a = 0.1 mm to a = 1 mm, to study the effect of source width on the visibility of the diffraction fringes.

The experimental results corroborate the theory presented earlier, demonstrating that diffraction from a phase step can be used to measure both the width of the light source and the transverse coherence length. The decrease in fringe visibility with increasing source width and the calculated relationship for the transverse coherence length agree with theoretical values, thus validating the proposed methodology.

2.11 Measuring Phase Shifts in Optical Fibers

The study describes how the optical path difference (OPD) of light, which depends on the angle of incidence, the refractive index of the plate and the surrounding medium, and the wavelength of the light, influences the diffraction fringes. By plotting the intensity of the diffraction fringes against the OPD, this method can be used to measure phase changes by varying the angle of incidence, as shown in Equation (2.19), where I_{N_j} is the normalized intensity of the diffraction fringes for λ and $\lambda/2$ [20].

The authors applied this technique to measure the phase shift imposed by the refractive index profile of a single-mode optical fiber. The demonstrated technique is reliable and precise for measuring phase changes and refractive index profiles.

In summary, the work proposes a phase shift calibration method based on Fresnel diffraction to measure phase changes in various optical contexts, including the evaluation of optical fibers.

$$\varphi = \kappa\delta = 2\sin^{-1}\left(1 - I_{N_j}\right) \ . \tag{2.19}$$

For the experiment, a cell with dimensions of $25 \times 25 \times 2$ mm^3 was constructed using two glass slides to introduce an index-matching liquid into the cell. The liquid was composed of 87% dimethyl sulfoxide and 13% distilled water. Inlets and outlets were prepared for a single-mode optical fiber with a diameter of 0.125 mm through the cell, as shown in Figure 2.12. The single-mode optical fiber was placed in the path of a monochromatic laser beam with a wavelength of λ =632.8 nm, and positioned using a microscope objective such that the light incident on its axis was perpendicular. The parallel beams exiting the objective illuminated a microscope glass slide with dimensions of $22 \times 22 \times 0.2$ mm^3, with the transparent plate parallel to the slide. The plate was mounted on a holder that could be rotated with a precision of 1 arc minute. The diffraction patterns of the light diffracted from the plate were recorded using a commercial CCD camera.

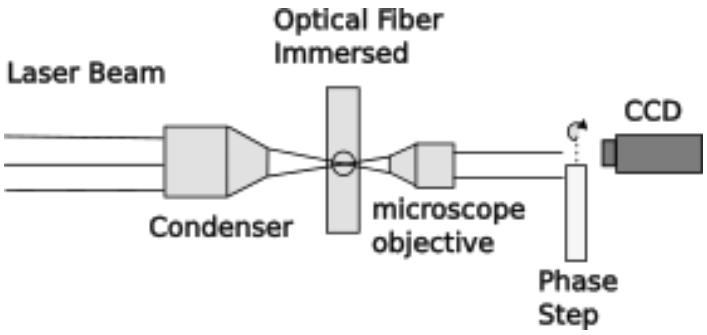

Figure 2. 12. Sketch of the experimental setup for measuring phase shifts in optical fibers.

The OPD of the light transmitted through the fiber changes, modulating the diffraction fringes along the edge of the plate. To measure the phase shift imposed by the optical fiber, diffraction patterns were recorded in the presence of the fiber, and then the fiber was gently removed to record a series of consecutive patterns

while rotating the plate. The intensity of the central dark fringe in the recorded diffraction patterns was measured, and the normalized intensity of the fringe was obtained for each pattern.

The phase shift results from the phase difference between the light passing through the left and right sides of the plate's edge, which is obtained using Equation (2.19). The minimum distance from the plate's edge must be $\Delta y = d_{co} \cos\alpha'$, which in the experiment is approximately 9 μm. d_{co} is the core fiber's diameter and α' is the intersection angle between the fiber and the plate's edge.

The study highlights the effective use of Fresnel diffraction to calibrate and measure phase shifts in optical fibers. Potential sources of error were identified, such as CCD dark current and variations in the index-matching solution. Measures were implemented to mitigate these errors, such as calculating and subtracting the background phase. The method proved practical and cost-effective, with less sensitivity to environmental vibrations than other approaches. The results were presented with error bars for precise comparison with conventional methods.

2.12 Quantitative Phase Imaging Using Scanning Diffractometry

A simple methodology is introduced for obtaining quantitative phase images without interference using scanning diffractometry [21]. The setup includes a low-coherence light beam passing through a condenser lens and focused on the microscopic sample, which is mounted on a computer-controlled translation stage to allow precise scanning of the sample. The light diffracted from the sample is collected by a microscope objective and directed towards a camera after passing through a transparent phase step (TPS) in transmission mode, placed 5 mm from the camera.

As the sample is scanned in front of the objective, the additional phase imposed by the section of the object in the optical axis transforms the TPS into a phase step with a different height. This height difference corresponds to the phase change of the sample and is extracted from the Fresnel diffraction patterns recorded by the camera, as described by Equation (2.20). The intensity distribution of the diffraction pattern is analyzed using Fresnel integrals, and the visibility is obtained to determine the phase changes and height of the sample. It is known that visibility is a periodic function of the TPS height.

$$\Delta\varphi = \frac{2\pi}{\lambda} h n_m \left[\sqrt{\left(\frac{n_{TPS}}{n_m} \right)^2 - \sin^2 \theta_i} - \cos\theta_i \right] \tag{2.20}$$

where n_{TPS} and n_m are the refractive indices of the TPS material and the surrounding medium, respectively.

In addition to the visibility, the positions of the minima and maxima in the diffraction pattern are analyzed. This parameter called the "extrema position parameter" (η), is defined by Equation (2.21).

$$\eta = \frac{x_{C\min}}{x_{R\max} - x_{L\min}} \tag{2.21}$$

where $x_{\min}$ and $x_{\max}$ are the positions of the minima and maxima of the fringes, respectively, on the left ($L_{\min}$), right ($L_{\max}$), and center ($C_{\min}$). The variation of η with changes in height is approximately linear, allowing for robust phase change measurements.

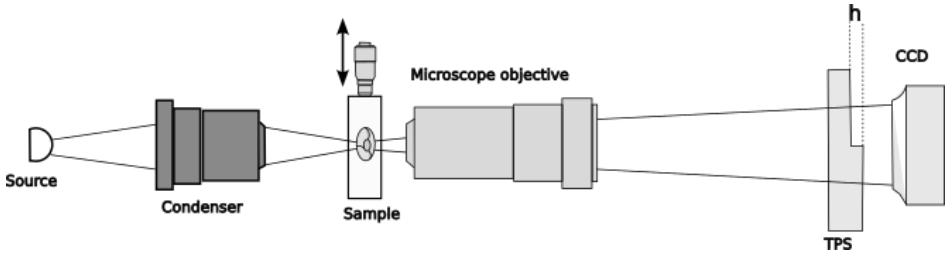

Figure 2. 13. The experimental setup of quantitative phase imaging using scanning diffractometry. It provides a straightforward and effective method for quantitative phase imaging.

In this work, a condenser lens is used to focus the light beam onto the sample Figure 2.13. The setup includes a 40x microscope objective, a camera with a resolution of 1024×1280 pixels and a pixel size of 5.2 μm, and a transparent phase step (TPS) fabricated by physical vapor deposition of an MgF_2 film with a thickness of 2.2 ± 0.04 μm.

The sample is positioned around the focal plane of the microscope objective, and the distance between the objective's back aperture and the TPS is approximately 30 cm. This ensures proper projection of the sample onto the TPS. During the scanning of the sample, the additional phase imposed by the section of the sample in the optical axis transforms the TPS into a phase step with a different height.

The proposed method for quantitative phase imaging via diffractometry offers a simple and effective configuration capable of measuring phase changes in microscopic samples with high precision. The described techniques provide a powerful tool for advanced studies in biomedicine and other scientific disciplines.

2.13 Fresnel Diffraction of Cylindrical Wavefronts at Phase Plate Edges

Fresnel diffraction of a cylindrical wavefront from the edge of a phase plate occurs when a cylindrical wave hits the edge of a transparent plate, causing a sharp phase change. The resulting phase difference varies continuously along the edge, and by using the Fresnel-Kirchhoff integral, the amplitude of the diffracted light in the Fresnel approximation can be determined. The phase distribution in the observation plane is a linearly varying function of the squared position, influenced by the light's wavelength, plate thickness, refractive index, and wavefront curvature. This creates a periodic intensity pattern along lines parallel to the edge, allowing for precise single-shot measurements of various optical parameters. Theoretical and experimental results show that the phase distribution is linear to the squared position and independent of the plate's position, validating the method's effectiveness in measuring wavefront curvature and displacement.

In the study of Fresnel diffraction (FD) from a line source at the edge of a transparent plate, a monochromatic cylindrical wave, with its symmetry axis perpendicular to the plane, strikes a plane-parallel plate near its upper edge. The plate is positioned at a distance z_0 from the source point S, with the edge perpendicular to the symmetry axis. When the wave transmits through the plate, it undergoes a phase change at the plate's boundary. The phase distribution on the $x'y'$ plane, immediately after the plate, is determined by considering rays that either propagate above the plate or pass through it at an incident angle θ, as shown in Figure 2.14.

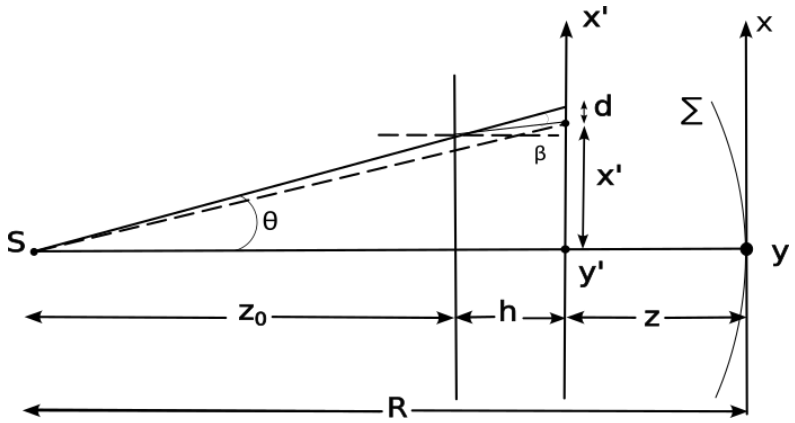

Figure 2. 14. Geometry used to calculate the optical Fresnel diffraction of cylindrical and spherical waves from a phase plate.

The phase distribution is given by:

$$\varphi(x'y') = \begin{cases} k\left(z_0\left(1+\dfrac{\theta^2}{2}\right)+nh\left(1+\dfrac{\theta^2}{2n^2}\right)\right), & y'<0 \\ k\left((z_0+h)\left(1+\dfrac{x^2}{2(z_0+h)^2}\right)\right), & y'>0 \end{cases} \tag{2.22}$$

For mathematical details review [15]. The normalized intensity provides a phase-shifting technique for optical measurements, showing periodicity along lines parallel to the plate edge (x -direction). As $\varphi(x)$ changes by 2π , the intensities repeat perpendicular to the plate edge (y -direction). The phase φ is a linear function of x^2 , dependent on light wavelength, plate thickness, refractive index, and Radius of Wavefront Curvature (RWC).

To evaluate the simulations presented and measure the RWC, Ghoorchi, and Dashtdar conducted experiments using a He-Ne laser with a wavelength of 632.8 nm, focused on a slit by a cylindrical lens, which then struck the edge of a 7.518 mm thick BK7 glass plate with a refractive index of 1.5151. The plate was aligned normally to the optical axis, and the resulting diffraction patterns were recorded by

a CMOS sensor connected to a computer. The sensor, mounted on a translation stage, captured the diffraction pattern at a distance of about 140 mm from the focal plane. By analyzing the phase difference of the fringe minimums along the plate edge and fitting the data to theoretical equations, the RWC was determined with high precision. The experiment was repeated with the sensor displaced by 20.0 mm, and consistent RWC measurements confirmed the method's accuracy. Additional experiments with a spherical wavefront showed similar results, validating the technique for different wavefront shapes. The phase distribution along the plate edge remained consistent even when the plate was displaced along the optical axis, demonstrating that the RWC measurement is robust against changes in plate position. This method provides a precise and straightforward approach to determining RWC and can be applied to quantitative phase imaging and studying material inhomogeneities.

3. Analytical description

As shown in the previous chapter, the phase step generates a diffraction pattern that can be used to develop relatively simple systems for its study and to obtain various applications. In this section, we will see the analysis necessary for the study of this phenomenon with a phase step in transmission mode and compare it with the FGSI method, in the measurement of glucose in water.

3.1 Diffraction of a phase step in transmission

In the literature, it is found that in most applications where a phase step is used to study diffraction, the laser beam is converted into a plane wave because it simplifies the study. In this section, we will examine the behavior of the phase step in transmission mode when it is in a medium with a given refractive index, and a plane wave propagates in that medium and transmits over the phase step. All calculations were simulated using the Fresnel integral, shown in the following Equation (3.1)

$$\Psi(x) = \frac{1}{\sqrt{i\lambda z}} \exp\left(i \frac{2\pi}{\lambda} z \right) \int \Psi(s) \exp\left(i \frac{\pi}{\lambda z} (x - s)^2 \right) ds \qquad (3.1)$$

$\Psi(s)$ is the wavefront, λ represents the wavelength of the local medium, and z propagates a distance, within the region of propagation. The limits of integration over the parameter s correspond to the region of illumination which, in the case of a Gaussian wavelet, are ± infinity [31-32].

Figure 3.1 depicts a one-dimensional thin transparent plate with a width L_P partially immersed in a homogeneous medium with a refractive index n_1. The thin plate is placed at an initial plane and has a refractive index n_2. The initial plane has coordinate x. A plane wave propagating in a direction parallel to the optical axis z illuminates a central region of a width D of the initial plane. A plane of observation, parallel to the initial plane, with coordinate x_F is placed at a distance z, with $z >> L_P$, as depicted in Figure 3.1.

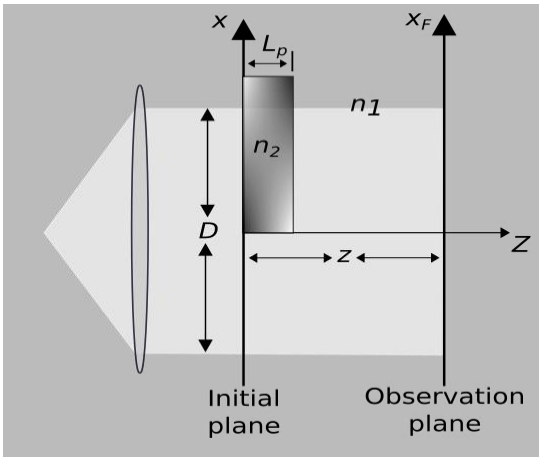

Figure 3. 1. Plane wave illuminating a transparent plate.

The amplitude distribution at the plane of observation with coordinate x_F can be calculated by using the Fresnel diffraction integral, Equation (3.1), as follows,

$$\psi_F\left(x_F\right)=\frac{A}{\sqrt{i\lambda_0 z/n_1}}\exp\left(i\frac{2\pi}{\lambda_0}n_1L_P\right)\exp\left(i\frac{2\pi}{\lambda_0}n_1 z\right)\int_{-D/2}^{0}\exp\left(i\frac{\pi}{\lambda_0 z}n_1\left(x-x_F\right)^2\right)dx$$

$$+\ \frac{A}{\sqrt{i\lambda_0 z/n_1}}\exp\left(i\frac{2\pi}{\lambda_0}n_2L_P\right)\exp\left(i\frac{2\pi}{\lambda_0}n_1 z\right)\int_{0}^{D/2}\exp\left(i\frac{\pi}{\lambda_0 z}n_1\left(x-x_F\right)^2\right)dx \tag{3.2}$$

In Equation (3.2), A is the amplitude of the illuminating plane wave.

After integration, Equation (3.2) can be expressed as,

$$\psi_F\left(x_F\right)=\frac{1}{q}\frac{A}{\sqrt{i\frac{\lambda_0}{n_1}z}}\exp\left(i\frac{2\pi}{\lambda_0}n_1 z\right)\exp\left(i\frac{2\pi}{\lambda_0}n_1L_P\right)$$
$$\times\left\{\begin{array}{l}\left[F\left(-qx_F\right)-F\left(-q\left(\frac{D}{2}+x_F\right)\right)\right]\\ +\exp\left(i\varphi\right)\left[F\left(q\left(\frac{D}{2}-x_F\right)\right)-F\left(-qx_F\right)\right]\end{array}\right\}. \tag{3.3}$$

In Equation (3.3), $q=\sqrt{\frac{2n_1}{\lambda_0 z}}$ and $\varphi=\frac{2\pi}{\lambda_0}\left(n_2-n_1\right)L_P$. The function $F\left(z\right)$ is equal to $C\left(z\right)+iS\left(z\right)$, where, the Fresnel cosine and sine functions are defined as,

$$C\left(z\right)=\int_0^Z\cos\left(i\frac{\pi}{2}t^2\right)dt,\qquad S\left(z\right)=\int_0^Z\sin\left(i\frac{\pi}{2}t^2\right)dt. \tag{3.4}$$

In Figure 3.2 we show normalized intensity profiles obtained with $F(z)$ in Figure 3.2(a) and with FGSI in Figure 3.2(b), for the propagation of the setup shown in Figure 3.1, with $n_1=1.3317088$, $n_2=1.5006$, $D=2.0$ cm, $L_P=1.0$ mm, and $z=40$ cm.

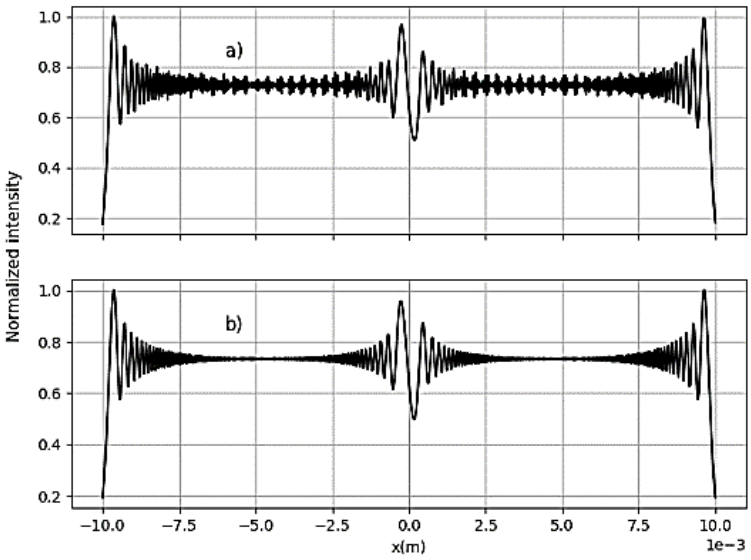

Figure 3. 2. Normalized intensity profiles due to the Fresnel diffraction from the transmission phase step of Figure 3.1. The plots were obtained by using, a) $F\left(z\right)$ and b) FGSI.

Figure 3.2 demonstrates the accuracy of the calculations obtained with FGSI which, additionally, provides a cleaner intensity profile compared with $F\left(z\right)$. In [33], it is demonstrated that calculations performed with $F\left(z\right)$ exhibit noisy distributions as z decreases. This effect can be expected upon analyzing the quadratic phases in the integrals of Equation (2.2) which oscillate more rapidly as z decreases. Hereafter, a small interval, around $x = 0$, along the x-axis, where the central ripples occur, will be referred to as the region of interest.

In the following sections, we will examine applications of diffraction from transmission phase steps utilizing FGSI.

3.2 Optical Setup for Measuring Glucose Concentration in Distilled Water Using FGSI: Analysis and Improvements

In addition to the applications mentioned in Chapter 2, recent applications [34 - 35] have been made for measuring glucose concentration in distilled water, which is the study we focus on to examine the diffraction phenomenon due to a phase step in transmission mode described in one dimension. We will start by describing the setup, referring to Figure 3.3.

A portion of a thin transparent plate is immersed in a container that has a width L_C = 10 cm and contains the liquid sample under inspection. The thin plate has a width L_P = 1.0 mm and a refractive index n_2 of approximately 1.5006. Its bottom edge is located at $x = 0$. A coherent collimated beam with wavelength λ_0 = 632.8 nm, propagating from the left, illuminates the front surface of the container through an aperture of width D. The front surface of the container is placed at a distance D_A =1.0 cm from the initial plane. The intensity distribution of the beam after being transmitted through the setup is recorded at a plane of observation placed at a distance D_B = 25 cm from the back surface of the container.

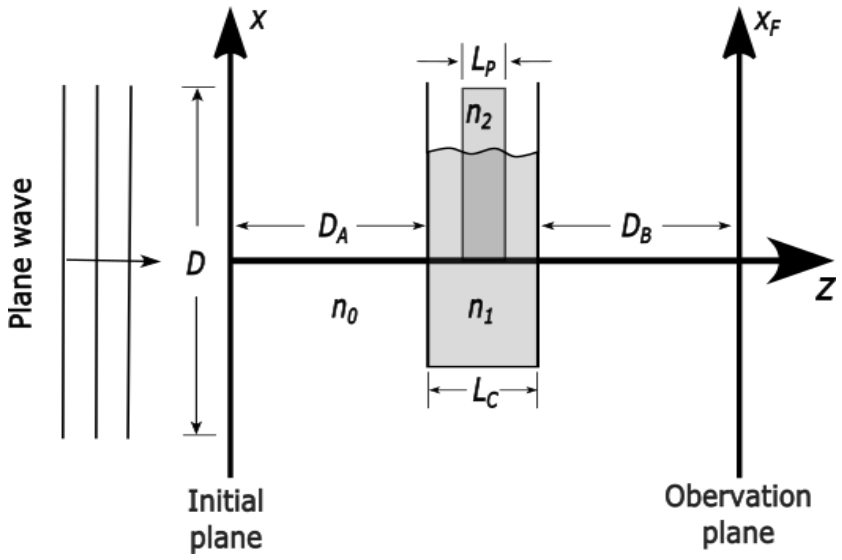

Figure 3. 3. Setup used in reference [34] as described in the text. A plane wave traveling through an aperture of width D in the air with a refractive index n_0 , illuminates a transparent, homogeneous medium with a refractive index n_1 in which a transparent thin plate with width L_P and refractive index n_2 is immersed. The initial and observation planes have coordinates x and x_F respectively.

We applied FGSI to calculate the propagation at the plane of observation to the setup depicted in Figure 3.3, n_0 , n_1 and n_2 represent the refractive indexes of air, the solution under measurement, and the thin plate respectively. The illuminating aperture has width D . It should be noted that all distance and width parameters of the plane wave were found by trial and error, as they are not mentioned in the reference. In Figure 3.4 we provide corresponding normalized intensity profiles in the region of interest for an aperture width D = 2.0 cm, centered at x = 0, for glucose concentrations 0, 10, 20, and 30 mg/dl, For the calculations, L_P =1.0 mm, L_C =10.0 cm, D_A = 1.0 cm, D_B = 25.0 cm, r_0 =0.4 mm and λ_0 = 632.8 nm.

To relate the refractive index of the surrounding medium, n_1 , with glucose concentration, we will follow [35] where it was found experimentally that in a range between 0 and 400 mg/dl, the refractive index can be written as,

$$n_1 = 1.3317078 + 1.515 \text{x} 10^{-6} \text{C} \, . \tag{3.5}$$

In Equation (3.5) the first term corresponds to the refractive index of pure distilled water at 25^0C and the parameter C corresponds to the concentration. Equation (3.5) indicates that the refractive index of the surrounding medium increases with concentration.

We did not conduct experiments for the setup depicted in Figure 3.3, as the corresponding experimental results are available in reference [34]. Instead, we emphasize that the graphs shown in Figure 3.4, obtained numerically with FGSI, fit well with the corresponding intensity distributions provided in the reference.

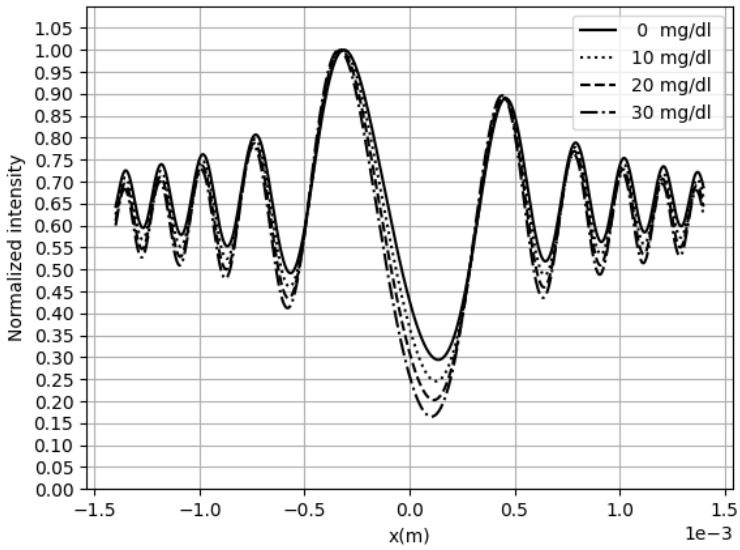

Figure 3. 4. Normalized intensity profiles obtained with FGSI for the setup of Figure 2.4. A plane wave travels through an aperture with a width of D = 2.0 cm for glucose concentrations 0, 10, 20, and 30 mg/dl. As the concentration increases, the minimums of the plots approach zero. For the calculations, L_P *=1.0 mm,* L_C *=10.0 cm,* D_A *= 1.0 cm,* D_B *= 25.0 cm,* r_0 *=0.4 mm and* λ_0 *= 632.8 nm.*

Figure 3.4 shows that, as the concentration increases, the minimum values of the plots approach zero. We have found that this excursion continues until the minimums reach zero and begin to increase again until reaching a maximum value and diminish again in a cyclic manner. Therefore, we have found that this cyclic

behavior causes the replication of graphs at different concentrations. For example, we have verified that graphs corresponding to concentrations 0.0, 418.0, and 836.0 mg/dl are strictly equal in the region of interest. This cyclic behavior represents a disadvantage, especially for clinical applications. Therefore, this method requires the support of auxiliary techniques to distinguish between different ranges of concentration.

Aside from our above finding, which represents a drawback, it is necessary to decrease the container width and replace the plane wave with a narrower beam to use the minimum possible amount of sample to permit extending the applicability of the method for clinical purposes. We want to demonstrate that performing these two changes will not deteriorate the sensitivity of the measurements.

3.3 Experimental measurements

The experimental setup in this section corresponds to the one depicted in Figure 3.3, with the illuminating plane wave replaced by a Gaussian beam obtained from a commercially available He-Ne laser, with a semi-width r_0 of approximately 0.4 mm and a wavelength λ_0 of 632.8 nm. This beam maintains its narrowness up to some moderate distances of propagation. For example, we can use Equation (3.1) to verify that this beam will exhibit a semi-width of 0.43 mm after propagating a distance of 53.0 cm, which will correspond to our setup to $D_A + D_B$. We set D_A = 22.0 cm and D_B = 31.0 cm. For the phase step, we have used a transparent thin plate with an optical quality λ/20. We have estimated the values for the width and refractive index of the thin plate as 1.02273 mm and 1.473894, respectively. To record the intensity profiles at the plane of observation we used a Pixelink PL-B762U CCD. The pixel pitch = 6.0 μm and resolution=752 x 480 (0.4 MP).

First, the Gaussian beam was verified using the CCD camera to ensure that the measurements made did not have any noise unrelated to the diffraction of the phase

step. Figure 3.5 shows the theoretical and experimental profile for the Gaussian beam.

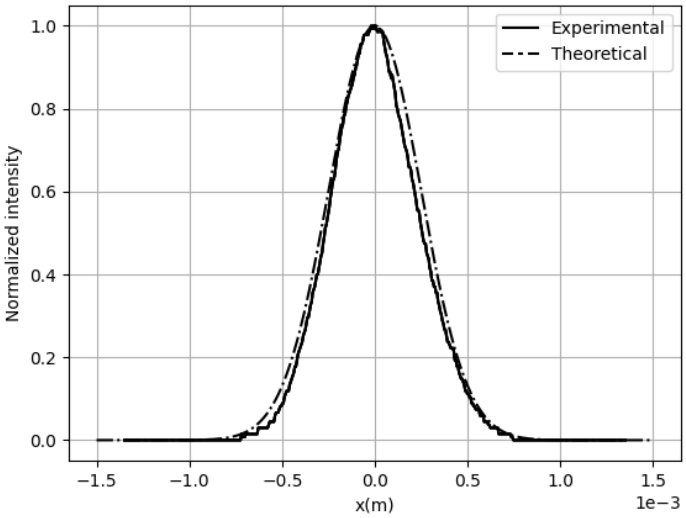

Figure 3. 5. Comparison of the Gaussian beam obtained with the CCD and a simulated beam.

Tests were also conducted to verify that temperature changes in the laboratory did not affect the measurements, as the system is sensitive to changes of up to approximately 3°C. The temperature in the laboratory ranges between 24°C and 27°C, which ensures that the measurements for this system will be reliable. Figure 3.6 shows a graph of 10 measurements taken every half hour.

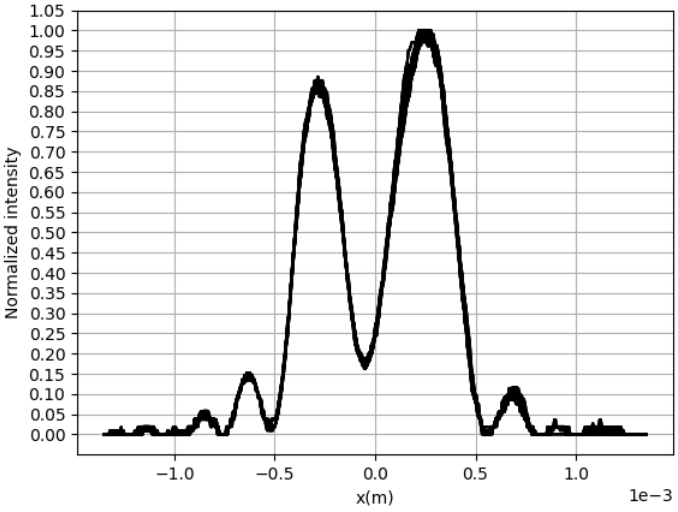

Figure 3. 6. Measurements of the diffraction due to a phase step. Ten measurements were taken over 5 hours, showing that the laboratory temperature is stable for conducting the experiments.

We will decrease the container width to accomplish the task mentioned at the end of the above section. In our experiments, the container width is 3.0 mm which represents a drastic reduction compared with the 10.0 cm width used in reference [34].

For the measurements, the medium inside the container will have the following refractive indexes: 1.3317078, 1.33172295, 1.3317381, 1.33175325, 1.3317684, and 1.33178355, which correspond to liquid, transparent solutions of distilled water with glucose concentrations ranging from 0 to 50 mg/dl in steps of 10 mg/dl, respectively, according with Equation (3.5). Figure 3.7 shows normalized intensity profiles, at the plane of observation, due to the illuminating Gaussian beam described above, transmitted through the optical setup. The plots correspond to the experimental measurements and their corresponding ones obtained with FGSI [37].

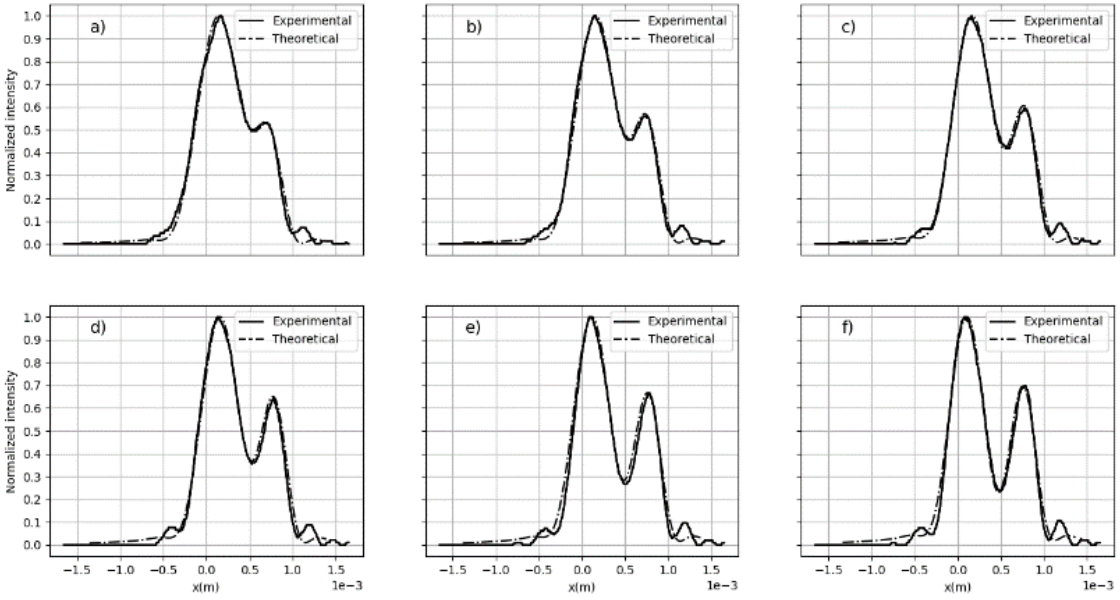

Figure 3. 7. Experimental and theoretical normalized intensity profiles at the observation plane. The illuminating beam is a Gaussian beam. Plots a)-f) correspond to the refractive indexes in the order listed in the text.

At the initial plane, the illuminating Gaussian beam had a slight tilt of 0.04°. The positions of the bottom edge correspond to x = 99, 105, 110, 117, 134, and 143 μm corresponding to Figures 3.7 a) – 3.7 f) respectively.

In practice, through simulation of the behavior of the phase step phenomenon, it was found that a Hermite-Gaussian (1,0) beam can be obtained by meeting certain distances. The Hermite-Gaussian beam $HG_{1,0}$ is characterized by its distinct intensity distribution, which has a single node along one of the transverse dimensions. This beam can be mathematically described by the product of a Gaussian function and a Hermite polynomial, resulting in an intensity profile with a central peak flanked by symmetric lobes. Such beams are often used in optical trapping and manipulation due to their unique focusing properties.

Since we do not have available this illuminating source, we have devised an alternative approach that closely resembles the desired beam. The approach consists of illuminating with a Gaussian beam a phase step made of a glass thin plate with surfaces of low optical quality. The width of the thin plate is approximately one-millimeter and its bottom edge is placed approximately at x =0 so that the upper half of the Gaussian illuminating beam is transmitted through the thin plate while the bottom half propagates freely. We can describe our approach with the help of the following Figure 3.3 as follows. Replacing the illuminating plane wave with two different sources, a Gaussian beam, and a Hermite–Gauss (1, 0) mode beam, denoted as $HG_{1,0}$. This beam may find applications where optical traps are used [36]. We obtained this beam using the Gaussian beam and an optical diffracting element. The amplitude of the $HG_{1,0}$ beam is given as,

$$HG_{1,0}(x,y) = C_1 H_1\left(\sqrt{2}\,\frac{x}{r_0}\right)\exp\left(-\frac{x^2+y^2}{{r_0}^2}\right). \tag{3.6}$$

In Equation (3.6), C_1 is a constant and H_1 is the first-order Hermite polynomial.

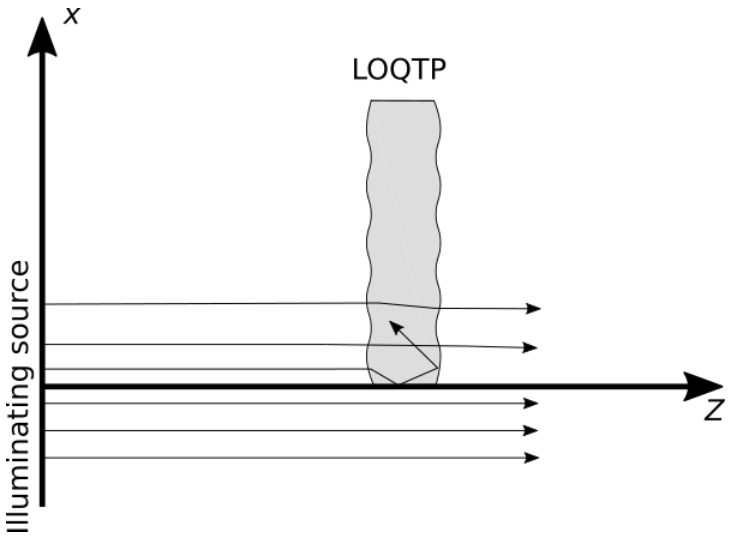

Figure 3. 8. Wavelets propagating through the low optical quality thin plate (LOQTP). The wavelet depicted near the bottom edge undergoes two total internal reflections; therefore, it does not reach the observation plane. The irregularities of the surfaces of the thin plate have been exaggerated for illustrative purposes.

In Figure 3.8, the illuminating beam is represented as a superposition of propagating wavelets, as suggested by FGSI. The figure shows six of these wavelets. The wavelets transmitted through the thin plate will undergo a small amount of tilt due to the irregularities of the walls, as depicted. In the figure, we have exaggerated the wavelet tilts and the irregular shape of the plate walls for illustrative purposes. Due to the random profile of the plate walls, it is possible to choose a zone where the wavelets that propagate near the bottom edge undergo two total internal reflections, therefore not reaching the observation plane. As a result, a central region of the transmitted beam resembles a $HG_{1,0}$ beam.

In Figure 3.9, we show gray level contours of the normalized intensity of the beam obtained in the manner described, propagated up to a plane of observation as recorded by the CCD, confirming our approach.

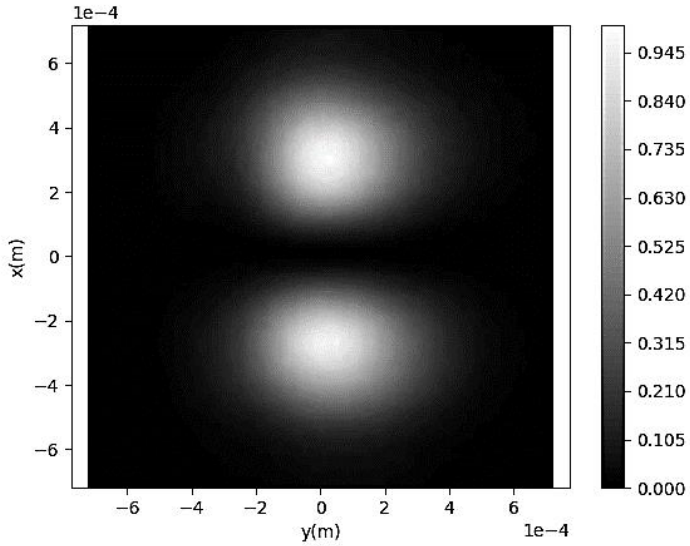

Figure 3. 9. Gray level contours of the normalized intensity distribution of a Hermite–Gauss (1, 0) mode beam obtained as described in the text, recorded by the CCD.

In Figure 3.10, we show the normalized intensity distribution that corresponds to a cut along $y = 0$ of Figure 3.9. It will be convenient now to compare the analytical equation of the $HG_{1,0}$ beam, propagated up to the plane of observation obtained with FGSI with the experimental one, obtained with the approach described above.

Figure 3.10 shows the corresponding one-dimensional normalized intensity profiles of both beams.

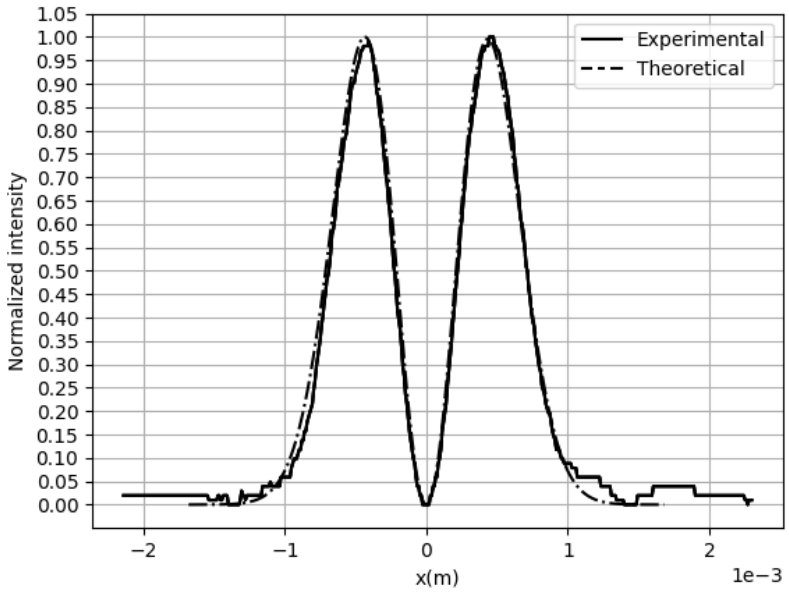

Figure 3. 10. Normalized intensity profile, at a plane of observation, of a cut along $y = 0$ *of Figure 3.9. For comparative purposes, the normalized intensity profile of a* $HG_{1,0}$ *beam obtained analytically with FGSI is also shown.*

Figure 3.10 shows the close resemblance of the beam, obtained with the approach described above, and the $HG_{1,0}$ beam. At x =0, its intensity distribution, for practical purposes, is zero. This characteristic is typical for this beam. Additionally, at approximately x = ±0.35 mm, the beam exhibits maximum intensity. For our following experiments, we will investigate the effect of illuminating the phase step with this beam for two cases: when the thin plate edge is at a x =0 and x =0.35 mm. To perform the experiments, the illuminating $HG_{1,0}$ beam obtained with the approach described above will illuminate the phase step as illustrated in the following Figure 3.11.

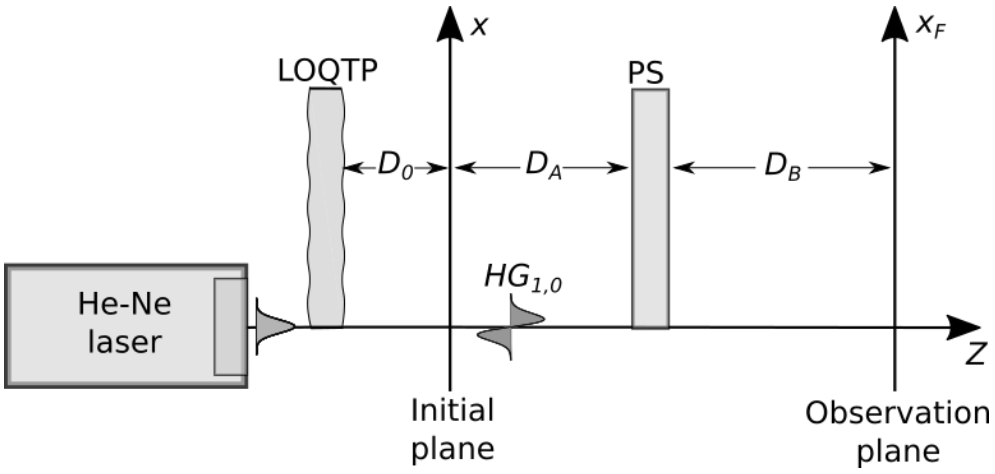

Figure 3. 11. $HG_{1,0}$ *beam obtained with the approach described in the text to illuminate the phase step (PS). LOQTP is a low optical quality thin plate.*

In Figure 3.11, the initial plane is placed at a short distance, D_0, from the LOPQT to separate it to fit within the Fresnel region, L_P =1.02261 mm, D_A =1.0 cm, D_B =25.0 cm. In addition, we confirmed that the $HG_{1,0}$ beam propagates appropriately within the zone between the initial and observation planes as set in our experiments.

The following Figures 3.12 (a) and 3.12 (b), show the corresponding experimental and theoretical normalized intensity profiles for two different positions of the thin plate edge, x = 0 and 0.35 mm. To better appreciate the effect, the figures include a gray bar which represents the location of the phase step for each case.

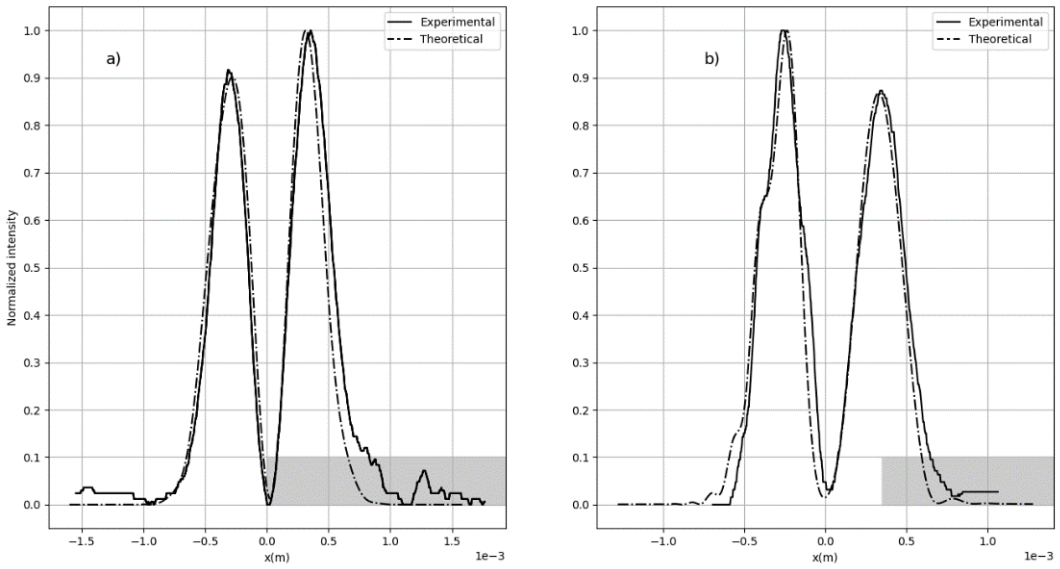

Figure 3. 12. Experimental and theoretical normalized intensity profiles at the observation plane for the illuminating obtained $HG_{1,0}$ *beam.* L_P *=1.02261 mm,* D_A *= 1.0 cm,* D_B *=25.0 cm. The gray bar represents the location of the bottom edge.*

By comparing the profiles of Figure 3.12 with Figure 3.10, one can observe that the thin plate has altered the distribution of the illuminating $HG_{1,0}$ beam for the two positions of the plate edge.

In addition to our findings described above, the accuracy of our theoretical results allows us to confirm the reliability of FGSI for calculating the overall diffraction that occurs through the optical setups analyzed. In the following section, we will take advantage of the reliability of FGSI to investigate more exhaustively appropriate conditions that will permit us to assess, analytically, the performance of the Fresnel diffraction from a phase step.

4. Numerical evaluation of the performance of the diffraction from a transmission phase step using FGSI.

From the work carried out and the results obtained, mentioned in the previous chapter, it was possible to discover that the phase step has an operating range, where a maximum sensitivity or zero sensitivity can be obtained. That is to say, it may be that we cannot obtain changes in the system depending on the refractive indexes and the thickness of the plate.

4.1 Normalized Sensitivity in Fresnel Diffraction Systems

Let us denote the normalized sensitivity of the system by the symbol S_e . To understand how S_e behaves, we will explore its dependence on the optical properties of the system. Specifically, we aim to demonstrate that S_e is characterized by a sinusoidal variation, which is governed by half the optical path difference (OPD) between adjacent wavelets. These wavelets propagate in a direction that is parallel to the bottom edge of the setup, traversing both the thin plate and the surrounding medium.

The optical path difference arises due to the difference in the refractive indices of the thin plate and the surrounding medium. As the wavelets travel through these materials, the phase shifts they experience lead to constructive and destructive interference patterns. These interference patterns are what ultimately determine the system's sensitivity.

By analyzing the propagation of these wavelets, we find that the normalized sensitivity S_e can be mathematically described as a sinusoidal function of half the OPD. This relationship highlights the periodic nature of the sensitivity to changes in

the optical path difference, which is crucial for understanding and optimizing the system's performance.

Analytically, this can be expressed as follows:

$$S_e = \left[\sin\left(\frac{1}{2}(OPD) \right) \right]^2 . \tag{4.1}$$

In Equation (4.1),

$$OPD = \frac{2\pi}{\lambda_0}(n_2 - n_1) L_P . \tag{4.2}$$

In Equation (4.2), n_1 and n_2 correspond to refractive indexes of the surrounding medium and the thin plate respectively.

Equation (4.1) indicates that the sensitivity is completely lost when OPD is a multiple of 2π. In contrast, the maximum sensitivity occurs for an odd multiple of π.

At this stage, it is important to analyze the influence of the parameter S_e on the measurements obtained from the setup depicted in Figure 3.11, particularly in response to changes in the refractive index of the surrounding medium. This analysis will provide deeper insights into how variations in S_e affect the accuracy and sensitivity of the system in detecting different glucose concentrations.

To illustrate this, Figure 4.1 presents a series of plots showing the normalized intensity profiles at the observation plane for four distinct glucose concentrations. These plots are essential for understanding the system's performance under varying conditions.

The figure includes graphs corresponding to the two extreme cases of sensitivity: the minimum sensitivity, when $S_e = 0$, and the maximum sensitivity, when $S_e = 1$. for different glucose concentrations 0, 10, 20, and 30 mg/dl for two different sensitivity values, $S_e = 0$ and $S_e = 1$ in a) and b) respectively.

By comparing these extreme cases, we can observe how the intensity profiles change with the refractive index variations caused by different glucose concentrations in the surrounding medium. This comparison allows us to evaluate the system's response and reliability in detecting changes in glucose concentration.

Through this analysis, we aim to demonstrate the critical role of the parameter S_e in the overall measurement process and highlight the system's capability to distinguish between different concentrations effectively. This understanding is crucial for optimizing the setup for precise and reliable measurements.

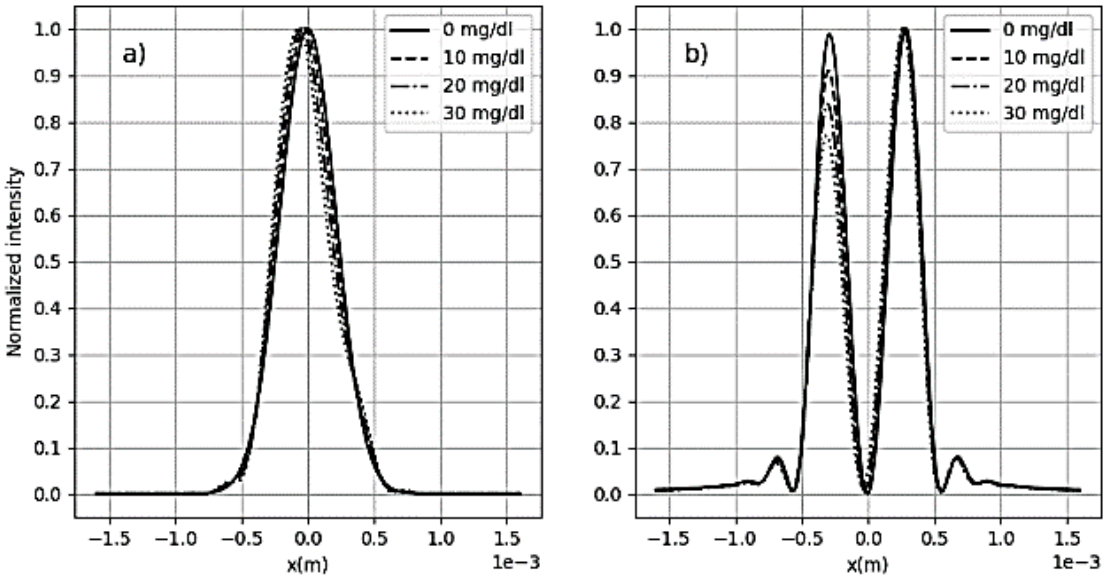

Figure 4. 1. Normalized intensity profiles for an illuminating Gaussian beam at different glucose concentrations and different sensitivity values. The normalized intensity profiles were performed for different glucose concentrations 0, 10, 20, and 30 mg/dl for two different sensitivity values, S_e = 0 and S_e =1 in a) and b) respectively. The peaks at x = - 0.35 decrease as glucose concentration increases.

Figure 4.1 (a) confirms that the changes in the recorded intensity profiles are negligible when $S_e = 0$.

It is important to observe that the profiles shown in Figure 4.1 differ significantly from those presented in Figure 3.7. This discrepancy arises from several factors. Firstly, in Figure 3.7, the sensitivity parameter S_e was set to an arbitrary value within the range of 0 to 1. This variability in sensitivity directly affects the intensity profiles, leading to the differences observed.

Additionally, another contributing factor is the slight tilt of the illuminating Gaussian beam used in the experiments depicted in Figure 3.7. This tilt introduces variations in the way the light interacts with the phase step and the surrounding medium, further altering the resulting intensity profiles.

Moreover, the positions of the bottom edge of the phase step differ between the two sets of figures. In Figure 3.7, the bottom edge is positioned at various locations, which impacts the diffraction pattern and the subsequent intensity profiles recorded at the observation plane.

These combined factors – the arbitrary sensitivity value, the tilt of the illuminating beam, and the varying positions of the bottom edge – contribute to the noticeable differences between the profiles in Figures 3.7 and 4.1. Understanding these variations is crucial for accurately interpreting the experimental results and for optimizing the setup to achieve consistent and reliable measurements.

To substantiate the aforementioned statement, we will closely examine the experimental setup illustrated in Figure 3.1. In this setup, n_1 represents the refractive index of the surrounding medium, while n_2 denotes the refractive index of the thin plate. Our objective is to analyze how slight changes in n_1 affect the overall system, particularly focusing on the parameter S_e which represents the normalized sensitivity of the system.

Initially, we will use Equation (3.5) to determine appropriate conditions that allow us to set n_1 to a specific initial value. It is important to note that the actual initial

value of n_1 is not crucial for this demonstration. The key point is to establish a baseline from which we can introduce controlled variations.

Once the initial value of n_1 is established, we will proceed by introducing small, incremental changes to n_1. During this process, all other parameters and conditions of the system will be held constant to isolate the impact of the changes in n_1. By doing so, we can accurately measure and calculate the resultant variations in the parameter S_e.

These induced variations in S_e due to the changes in n_1 will be quantified and analyzed. The goal is to demonstrate the sensitivity of the system to changes in the refractive index of the surrounding medium.

The corresponding calculation can be written as,

$$\frac{dS_e}{dn_1} = -\frac{\pi}{\lambda_0} L_P \sin\left(OPD\right) \ . \tag{4.3}$$

Equation (4.3) shows that the rate of change of S_e with respect to n_1 is proportional to L_P.

To confirm the aforementioned result, Figure 4.2 shows plots obtained using FGSI, for four different glucose concentrations and two different plate widths, approximately 1.0 and 2.0 mm. The illuminating beam is the same Gaussian beam described in the previous sections. The glucose concentrations range from 0 to 30 mg/dl in increments of 10 mg/dl.

In both plots, it is observed that the peak heights located approximately at -0.3 mm decrease as the glucose concentration increases. This trend is due to the interaction of the light beam with the glucose dissolved in the medium, which alters the observed diffraction pattern.

In plot a), corresponding to a plate width of approximately 1.0 mm, a clear decrease in the peak heights is noticeable as the concentration increases from 0 to 30 mg/dl. This behavior is repeated in plot b), which represents a plate with a width of approximately 2.0 mm, showing a similar trend but with differences in the amplitude of the peaks due to the greater thickness of the plate.

These observations are crucial for understanding how variations in plate width and glucose concentration affect the normalized intensity profile at the observation plane. The results obtained demonstrate the system's sensitivity to these changes, highlighting its potential application in detecting and quantifying glucose concentrations. The consistency of the results across different plate width configurations reinforces the validity of the method used and its capability to provide precise and reliable measurements.

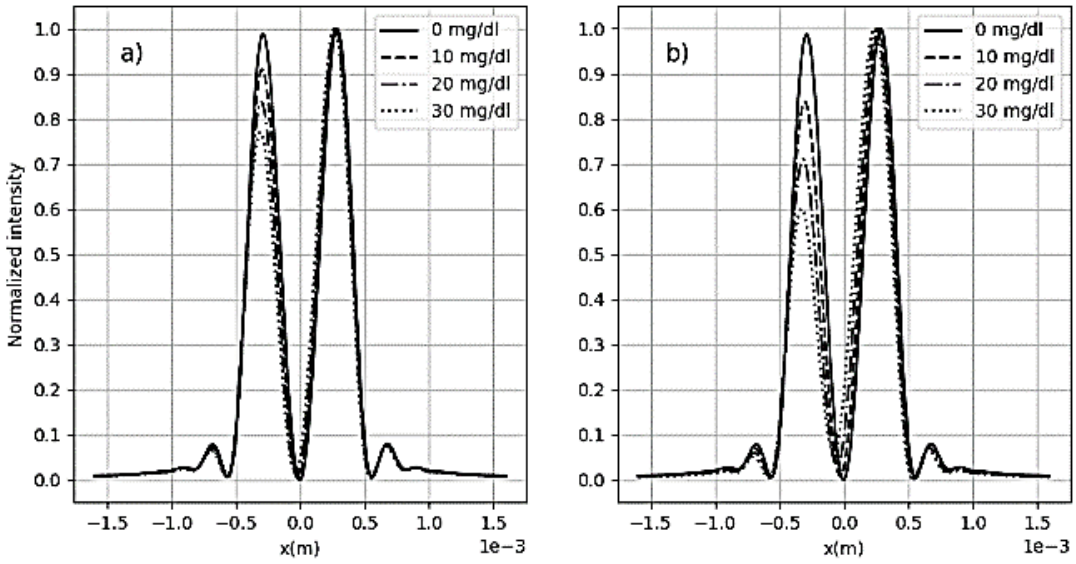

Figure 4. 2. Normalized intensity profiles calculated with FGSI. Normalized intensity profiles were calculated with FGSI due to an illuminating Gaussian beam for two thin plate widths of approximately 1.0 and 2.0 mm a) and b) respectively.

Figure 4.2 illustrates that the intensity profile corresponding to the thicker plate experiences greater variations due to changes in n_1, the refractive index of the surrounding medium. This observation is consistent with our expectations. The

thicker plate results in a longer interaction path for the illuminating beam as it passes through the interface between the plate and the surrounding medium. Consequently, even small changes in the refractive index n_1 lead to more pronounced variations in the intensity profile.

This characteristic highlights a fundamental principle: under equal sensitivity conditions, the extent of variation in the intensity profile is directly proportional to the length of the interaction path of the illuminating beam. Therefore, when the interaction path is longer, as is the case with the thicker plate, the system becomes more sensitive to changes in the refractive index. This increased sensitivity can be advantageous for applications requiring precise detection of small refractive index changes in the surrounding medium.

By carefully analyzing the intensity profiles for different plate thicknesses, we can better understand the influence of the interaction path length on the system's sensitivity. This understanding allows us to optimize the setup for specific applications, ensuring that the system can reliably detect and quantify changes in the refractive index with high accuracy.

4.2 Impact of system sensitivity for various beams

To confirm the validity of Equation (4.1), we will perform theoretical calculations using FGSI for four different illuminating sources with distinct spatial profiles. The profiles of the illuminating sources will be as follows: Gaussian, Hermite-Gaussian $HG_{1,0}$, $HG_{3,0}$, and Airy.

By employing these different illuminating sources in our theoretical calculations, we aim to thoroughly test the robustness and general applicability of Equation (4.1). Each beam profile will interact differently with the phase step and the surrounding medium, providing a comprehensive evaluation of the equation's validity under varying conditions. This approach will help ensure that the findings are not limited

to a specific type of beam but are applicable across a range of commonly used optical beam profiles. A brief description of the $HG_{3,0}$ and the Airy beams follows.

The amplitude distribution for the $HG_{3,0}$ beam is given as,

$$HG_{3,0}(x) = C_3 H_3\left(\sqrt{2}\frac{x}{r_0}\right)\exp\left(-\frac{x^2}{{r_0}^2}\right). \tag{4.4}$$

In Equation (4.4), C_3 is a constant and H_3 is the third-order Hermite polynomial.

The Airy beam is notable for its non-diffracting nature and its ability to maintain its shape over a long distance. The intensity profile of an Airy beam exhibits a main peak accompanied by a series of diminishing side lobes. This beam is described by the Airy function, which gives it a characteristic curved trajectory. Airy beams are of particular interest in applications requiring long-range beam propagation and precise control of the beam trajectory.

The corresponding amplitude distribution of an Airy beam can be written as $Ai(x/B)$, where B represents a constant scaling factor and Ai represents the Airy function. The Airy function is a solution to the following second-order linear differential equation [38]:

$$\frac{d^2}{dx^2}Ai(x) = x\,Ai(x). \tag{4.5}$$

where $Ai = {}^{1}\!/_{\pi}\int_0^{\infty}\cos\left({}^{t^3}\!/_{3} + xt\right)dt$.

The Airy function is known for its distinctive properties, including its non-diffracting behavior and ability to form self-healing beams. This function is central to the description of Airy beams, which exhibit a main intensity peak followed by a series of diminishing side lobes, providing a curved trajectory of the beam as it propagates.

These properties make Airy beams particularly useful in applications requiring precise beam control over long distances.

By incorporating the Airy beam profile into our theoretical calculations, we aim to validate Equation (4.2) under conditions where the beam exhibits unique propagation characteristics. The Airy function is available in SymPy, a free Python library for symbolic mathematics [39].

To calculate the propagation of the Airy beam, we use the Fresnel diffraction integral, Equation (2.2), and with the aid of the Fourier transform of Equation (4.5), one obtains a closed-form expression that permits writing the amplitude distribution of the propagated Airy beam at an observation plane with the coordinate x_F, as,

$$\begin{aligned} &\exp\left(i\frac{2\pi}{\lambda}z\right)\exp\left(-i\frac{2}{3}\left(\frac{\lambda z}{4\pi B^2}\right)^3\right) \\ &\times\ \exp\left(i\frac{\lambda z}{4\pi B^3}x_F\right)Ai\left(\frac{1}{B}\left(x_F-\frac{\lambda^2 z^2}{16\pi^2 B^3}\right)\right) \end{aligned} \quad . \tag{4.6}$$

In reference [30] a detailed description of the derivation of Equation (4.6) is provided.

Equation (4.6) explicitly demonstrates that the Fresnel diffraction integral has the remarkable property of preserving the unique characteristics of Airy beams. Specifically, it maintains the intensity distributions of these beams invariant during propagation. This preservation means that an Airy beam, when subjected to Fresnel diffraction, will retain its distinct intensity profile, which is a fundamental property that distinguishes Airy beams from other types of beams.

Furthermore, Equation (4.6) not only conserves the intensity distribution but also imparts the correct phase information necessary for the propagation of Airy beams. This phase information is crucial as it reflects the accelerating behavior that is a

hallmark of Airy beams. Unlike other beams that typically follow straight paths, Airy beams exhibit a parabolic trajectory, giving them the unique ability to accelerate during propagation.

It is important to note that Equation (4.6) was derived using a different analytical method in a previous study [41]. In that study, the preservation and propagation characteristics of Airy beams were analyzed without directly referencing the Fresnel diffraction integral. This independent derivation underscores the robustness and fundamental nature of the results encapsulated in Equation (3.2).

Moreover, the behavior of Equation (4.6) has been extensively studied in the context of truncated Airy beams. These experimental studies, as reported in [42], provide valuable insights into how truncated Airy beams—those with a finite extent—propagate and maintain their unique properties. The experiments confirm that even when an Airy beam is truncated, the core properties dictated by Equation (4.6) still hold to a significant extent. These studies are critical as they bridge the gap between theoretical predictions and practical implementations, demonstrating that the theoretical underpinnings are applicable in real-world scenarios.

In summary, Equation (4.6) is a powerful analytical tool that highlights the invariance of Airy beam intensity distributions under Fresnel diffraction. It also correctly predicts the phase evolution that gives rise to their accelerating behavior. This equation, corroborated by both independent analytical methods and experimental studies, provides a comprehensive understanding of the propagation dynamics of Airy beams, making it a cornerstone in the study of beam optics.

The following Figures 4.3 to 4.6 show calculations performed with FGSI of the Fresnel diffraction from a transmission phase step for the four illuminating sources listed above. For these simulations, we set the width of the phase step plate, denoted L_P , to be approximately 1.0 mm. This adjustment was crucial to ensure that the optical path difference (OPD) values were correctly aligned with the conditions necessary to achieve two different sensitivity settings, S_e = 0 and S_e = 1.

By carefully tuning these parameters, we attempt to accurately simulate diffraction effects and capture the phase step behavior under different lighting conditions. The figures clearly show how each type of beam interacts with the phase step, revealing the nuances of the diffraction patterns and providing insight into the optical phenomena at play.

These calculations serve as a comprehensive analysis and provide valuable data that can be used to better understand the effects of transmission phase steps in various optical systems.

The following Figure 4.3, corresponds to the illuminating Gaussian beam for three positions of the bottom edge and both sensitivities. The upper three plots correspond to an OPD that fits maximum sensitivity conditions; the three lower plots correspond to minimum sensitivity. The positions of the bottom edge correspond to x = - 0.3, 0.0 and 0.3 mm, D_A = 1.0 cm, D_B = 25.0 cm, r_0 = 0.4 mm and λ_0 = 632.8 nm. $L_P \approx$ 1.0 mm and adjusted to fit with the required OPD values. The gray bar indicates the position of the thin plate.

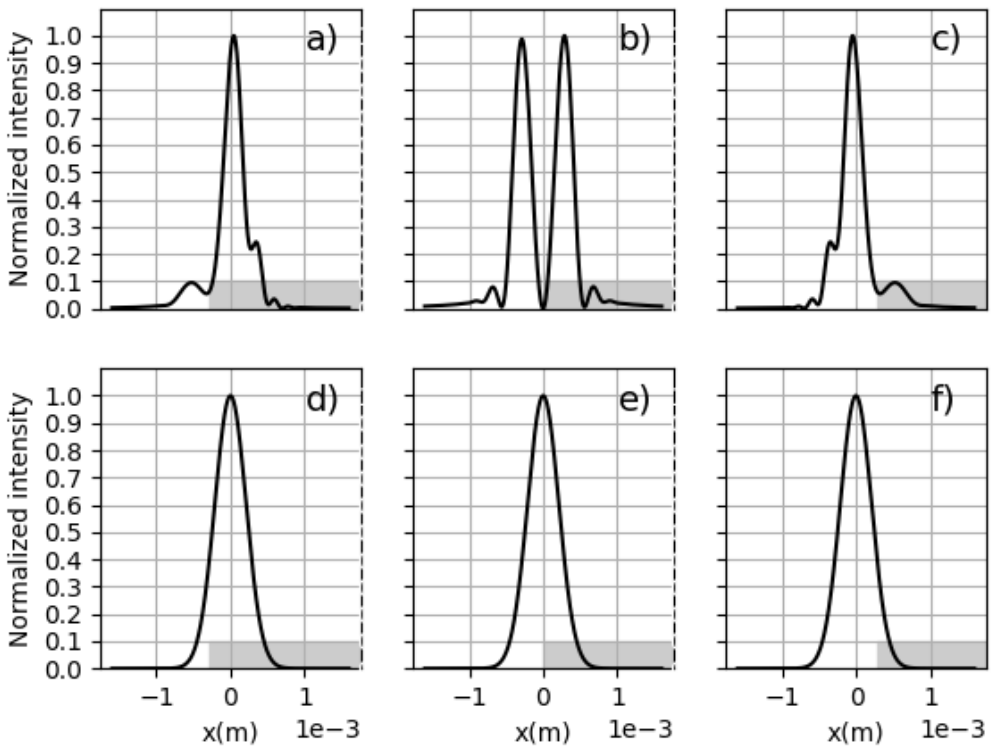

Figure 4. 3. Fresnel diffraction from a transmission phase step surrounded by pure distilled water and illuminated by a Gaussian beam. The upper three plots, a), b) and c), correspond to an OPD that fits maximum sensitivity conditions; the three lower plots, d), e) and f), correspond to minimum sensitivity. The positions of the bottom edge correspond to x *= - 0.3, 0.0 and 0.3 mm,* D_A *= 1.0 cm,* D_B *= 25.0 cm,* r_0 *= 0.4 mm and* λ_0 *= 632.8 nm.* $L_P \approx$ *1.0 mm and adjusted to fit with the required OPD values. The gray bar indicates the position of the thin plate.*

In Figure 4.4 we show plots corresponding to the illuminating $HG_{1,0}$ beam under the same conditions as for the Gaussian beam.

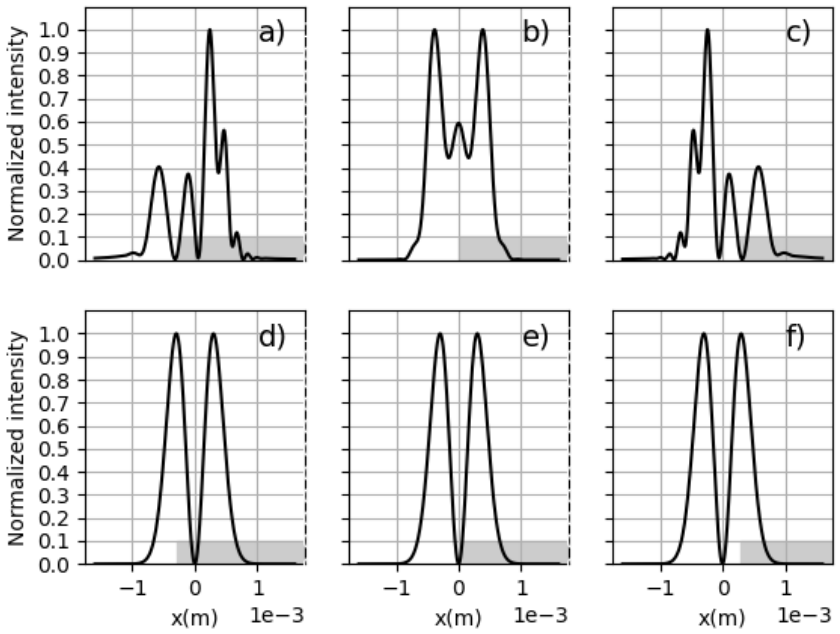

Figure 4. 4. Normalized intensity profiles due to the illuminating $HG_{1,0}$ beam, recorded under the same conditions as those in Figure 4.3. Maximum sensitivity conditions for a), b) and c), and minimum sensitivity conditions for d), e) and f).

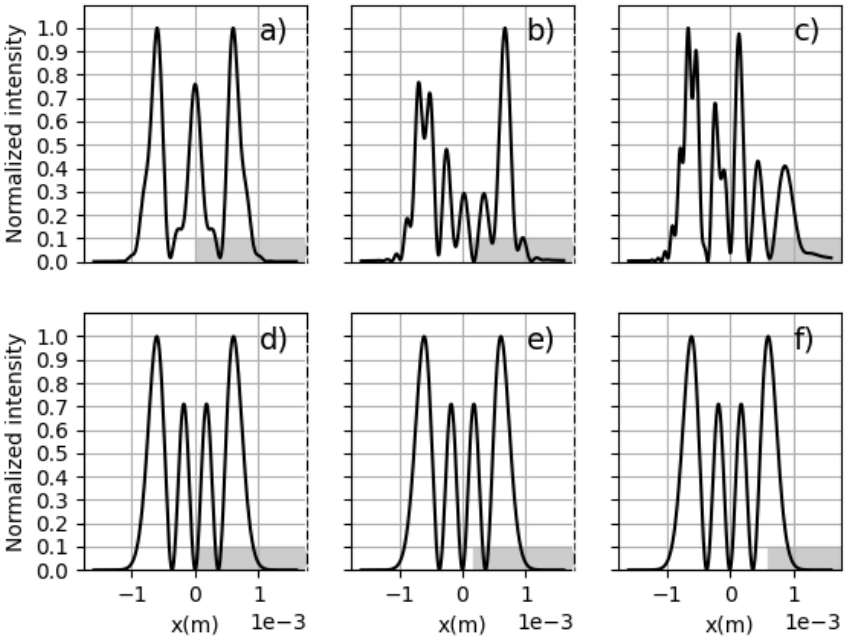

Figure 4. 5. Normalized intensity profiles of an illuminating $HG_{3,0}$ beam. The beam was recorded under analogous conditions as those in Figure 4.4. Maximum sensitivity conditions for a), b) and c), and minimum sensitivity conditions for d), e) and f). The positions of the bottom edge correspond to X = 0.0, 0.17, and 0.6 mm.

In Figure 4.5 we show plots for an illuminating $HG_{3,0}$ beam, analogous to the above cases, the positions of the bottom edge correspond to x = 0.0, 0.17, and 0.6 mm.

In Figure 4.6 we show the plots corresponding to the illuminating Airy beam, The positions of the bottom edge correspond to x = - 0.40, - 0.23, and - 0.10 cm.

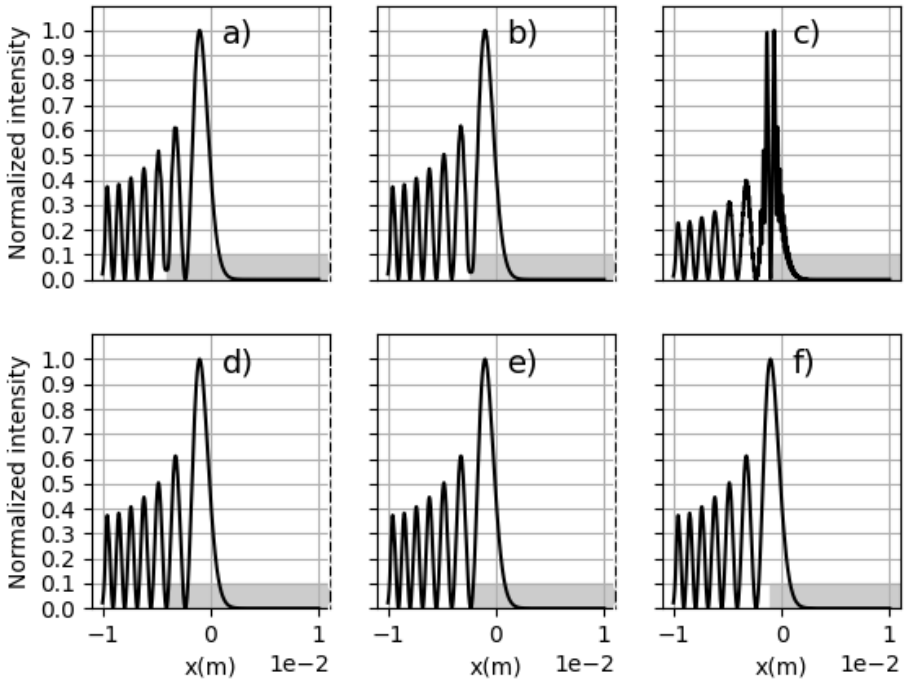

Figure 4. 6. Normalized intensity profiles due to the illuminating Airy beam. It was recorded under analogous conditions as those in Figure 4.5. Maximum sensitivity conditions for a),b) and c) , and minimum sensitivity conditions for d), e) and f). The positions of the bottom edge correspond to x = - 0.40, - 0.23 and - 0.10 cm.

Figures 4.3 to 4.6 illustrate the intensity profiles observed at the detection plane under conditions of minimum sensitivity S_e =0. These results highlight an important characteristic of the optical system: the intensity profiles remain undistorted even after passing through the transmission phase step. This implies that the phase step does not alter the intensity distribution of the beams when the sensitivity is set to its minimum value.

Additionally, the observed intensity profiles at the plane of observation are identical to those of the illuminating beams at the initial plane. This consistency between the initial and observed profiles confirms that the phase step, under minimum sensitivity conditions, does not introduce any significant diffraction effects or distortions. As a result, the integrity of the original beam profiles is maintained throughout the propagation process.

These findings are crucial as they validate the system's performance under low-sensitivity settings. By ensuring that the phase step does not affect the beam profiles, we can confidently use this setup for applications where maintaining the original beam characteristics is essential. The results demonstrate the robustness of the system in preserving the quality of the illuminating beams, which is a vital aspect for various optical experiments and applications.

Based on the plots presented in Figures 4.3 to 4.6, it is evident that the system's sensitivity is entirely lost when the Optical Path Difference (OPD) is a multiple of 2π, as anticipated earlier. In such instances, the intensity profile observed at the plane of observation remains unchanged regardless of the thin plate's position. Conversely, at points of maximum sensitivity (corresponding to odd multiples of π), the intensity profile does vary. This suggests that, from a physical standpoint, the primary interaction of light with the phase step predominantly occurs at the interface between adjacent wavefronts.

Additionally, Figures 4.6 a) and 4.6 b) demonstrate that the non-diffracting nature of the Airy beam remains dominant even when interacting with the phase step, including under conditions of highest sensitivity. When the edge of the thin plate aligns with a position where the Airy beam exhibits zero intensity, the entire intensity profile remains essentially unchanged for practical purposes. This unique behavior is not observed with other types of beams that also show zero intensity at specific positions. This distinction is confirmed through the analysis of Figures 4.3 and 4.4, where other beam types do not maintain an unaltered profile under similar conditions.

Furthermore, Figures 4.6 a) and 4.6 b) provide a revealing insight into the behavior of the Airy beam in the context of its interaction with the phase step. These figures clearly illustrate that the Airy beam's non-diffracting property remains predominant, even under conditions where the system is at its highest sensitivity. Specifically, when the edge of the thin plate is positioned at a point where the Airy beam's intensity is zero, the entire intensity profile remains virtually unchanged. This implies that, for all practical purposes, the presence of the phase step does not significantly alter the overall intensity distribution of the Airy beam.

This unique characteristic of the Airy beam contrasts sharply with the behavior of other types of beams. For these other beams, which also exhibit positions of zero intensity, the interaction with the phase step results in noticeable changes in their intensity profiles. This difference is substantiated by the data presented in Figures 4.4 and 4.5. These figures reveal that other beam types do not maintain a stable intensity profile when the edge of the thin plate coincides with a zero-intensity position. Thus, while the Airy beam's profile remains remarkably stable and unaffected by the phase step under certain conditions, other beams demonstrate a clear sensitivity to similar interactions, leading to altered intensity distributions.

Based on our findings, we can propose a novel scanning device designed to function as a thickness profilometer along the edge of a transparent plate. This device would utilize the setup illustrated in Figure 3.3, which is illuminated by a Gaussian beam. To achieve optimal sensitivity, we can finely adjust it to a value between 0 and 1. This adjustment can be easily accomplished by employing a liquid solution with a suitable glucose concentration as the surrounding medium. This will ensure that the height of one of the lobes is set to approximately half of its maximum value.

Figure 4.7 presents the intensity plots at the observation plane, obtained using the FGSI technique for four different thicknesses of the thin plate along its edge under these specified conditions. These plots demonstrate a clear relationship between the thickness of the plate and the resulting peak heights in the intensity profile. Specifically, the peaks shown in Figure 4.7 correspond to a plate with an initial

thickness of 1.0 mm, with subsequent increases in thickness in steps of 100 nm. As the thickness of the plate increases, there is a corresponding increase in the heights of the peaks.

This proposed scanning device offers a precise and reliable method for measuring the thickness of a transparent plate along its edge, leveraging the sensitivity and accuracy of the Gaussian beam setup and the tailored glucose concentration in the surrounding medium. The ability to detect incremental changes in thickness with high resolution makes this device an invaluable tool for applications requiring meticulous thickness profiling.

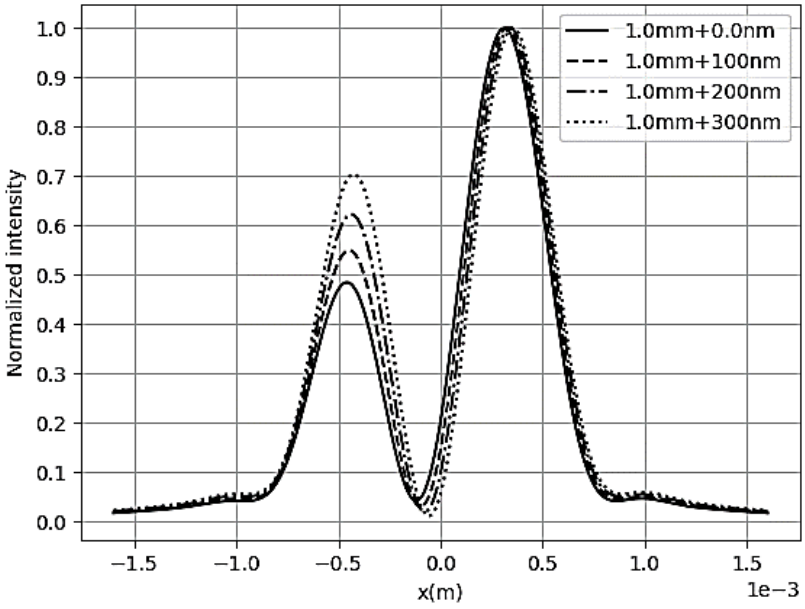

Figure 4. 7. Normalized intensity profiles for four hypothetical thicknesses of 1.0 mm + 0.0, 100.0, 200.0, and 300.0 nm. Along the bottom edge of a thin plate. As the width of the plate increases, the height of the left peaks increases.

The numerical results depicted in Figure 4.7 must be validated through rigorous experimental procedures to ensure their accuracy and reliability. This validation step is crucial for confirming the theoretical predictions and numerical simulations presented in this study. Before concluding this report, it is important to highlight

that the findings discussed herein are expected to be equally applicable to the case of reflection phase steps, as the underlying equations governing these phenomena are analogous to those for transmission phase steps.

To broaden the understanding of the physical interaction between the illuminating beam and the phase step, it is pertinent to mention recent advancements in the field. Specifically, it has been suggested that the diffracted wave generated at the discontinuity -precisely at the interface- can be described using a modulated probability function. This approach draws parallels with methods used in quantum mechanics, where such functions are employed to extract statistical information about particles. By applying this framework to the study of diffracted waves, researchers can gain valuable insights into the statistical behavior of the interacting photons. This perspective not only enriches our comprehension of the interaction dynamics but also opens up new avenues for exploring the quantum-like properties of light in classical optical systems. By considering the diffracted wave as a modulated probability function, we can better understand how light interacts with discontinuities at a fundamental level. This approach enables the extraction of detailed statistical information about the photons involved in the interaction, potentially leading to novel applications and techniques in both classical and quantum optics.

In summary, while the numerical results presented in this report provide a robust theoretical foundation, experimental validation is essential to confirm their validity. Additionally, the analogy with quantum mechanics offers a fascinating framework for further exploring the interaction of light with phase steps, providing a deeper understanding of the underlying physics and expanding the potential applications of this research.

5. Conclusions

We have developed and presented a straightforward experimental procedure to evaluate optical diffractometry using Fresnel diffraction from a transmission phase step. This procedure involves partially immersing a thin, high-optical-quality plate into differently calibrated glucose solutions, allowing precise variation in the refractive index of the surrounding medium. By employing this method, we can systematically control and observe the impact of changing refractive indices on the diffraction patterns produced.

Our experimental results have been meticulously compared with numerical calculations obtained using the Fresnel Gaussian Shape Invariant (FGSI) method. This comparison has demonstrated the accuracy and reliability of our procedure in numerically calculating the propagation of an illuminating field through optical setups containing phase steps. The precision of the FGSI method has been crucial in these calculations, ensuring that the results are both dependable and reproducible.

A key finding from our study is the behavior of the system's sensitivity related to the optical path difference between neighboring wavelets propagating parallel to the edge through the thin plate and the surrounding medium. Specifically, we have shown that the system completely loses its sensitivity when this optical path difference is a multiple of 2π. Conversely, the system exhibits maximum sensitivity when the optical path difference is an odd multiple of π. This sensitivity behavior is independent of the type of illumination used, underscoring the robustness of our findings.

Additionally, we have observed that the intensity variations at the plane of observation increase with the path length of the interaction of the illuminating beam at the interface of the phase step. This relationship highlights the importance of the interaction length in determining the intensity patterns observed in the diffraction setup.

To further substantiate our findings, we performed additional calculations for four different illuminating beams: Airy, Gaussian, and Hermite–Gaussian beams in the (1, 0) and (3, 0) modes. Our results indicated that the non-diffracting property of the Airy beam remained dominant even when interacting with the phase step. Specifically, when the edge of the thin plate coincided with one of the positions of zero intensity of the Airy beam, the entire profile of the beam remained unaltered, even under conditions of maximum sensitivity.

Based on the insights gained from our study, we have proposed a design for a high-resolution thickness profilometer. This device leverages the principles observed in our experiments to measure the thickness along the edge of a thin plate with high precision. The proposed profilometer holds significant potential for applications requiring detailed thickness measurements, particularly in fields such as metrology and material science.

6. Annex. Wave-front propagation with FGSI

FGSI is a numerical method utilized to calculate the diffraction of fields as they propagate through optical setups. This method represents the initial field as a superposition of Gaussian wavelets, which allows for a versatile and detailed analysis of various optical phenomena. The initial field can, in principle, be any real or complex field, making FGSI a highly adaptable tool for different types of optical studies.

Typically, the representation of the one-dimensional field at the initial plane involves between 200 and 1000 Gaussian wavelets. Each Gaussian wavelet's amplitude corresponds to the local complex amplitude of the field, and these wavelets are uniformly distributed across the initial plane. This uniform distribution and the correspondence of wavelet amplitudes to the local field values simplify the programming of the FGSI method. However, it is important to note that other

configurations and distributions are also possible, depending on the specific requirements of the study.

A brief description of the FGSI method is as follows:

1. Initialization: The initial optical field is represented by a superposition of Gaussian wavelets. Each wavelet has a specific amplitude and phase corresponding to the local complex amplitude of the field at the initial plane.

2. Wavelet Distribution: The Gaussian wavelets are uniformly distributed across the initial plane. This uniform distribution helps in simplifying the numerical implementation of the method.

3. Propagation: The propagation of each Gaussian wavelet through the optical setup is calculated using the appropriate diffraction integrals. This step involves computing the contribution of each wavelet to the field at subsequent planes within the optical setup.

4. Superposition: The contributions of all the Gaussian wavelets are summed to obtain the total field at each plane of interest. This superposition principle allows for the reconstruction of the field as it evolves through the optical setup.

5. Analysis: The resulting field is analyzed to extract relevant information, such as intensity profiles, phase distributions, and diffraction patterns. This analysis provides insights into the behavior of the optical system under study.

By using 1000 Gaussian wavelets, we ensure a detailed and accurate representation of the initial field, leading to precise calculations of the diffraction effects. The FGSI method's flexibility and adaptability make it a powerful tool for exploring complex optical phenomena and obtaining high-resolution results.

Figure A.1 shows one Gaussian wavelet, propagating through an optical setup. At the initial plane, the wavelet is directed at an angle θ_0. For simplicity, we focus on a one-dimensional model; extension to two dimensions is straightforward.

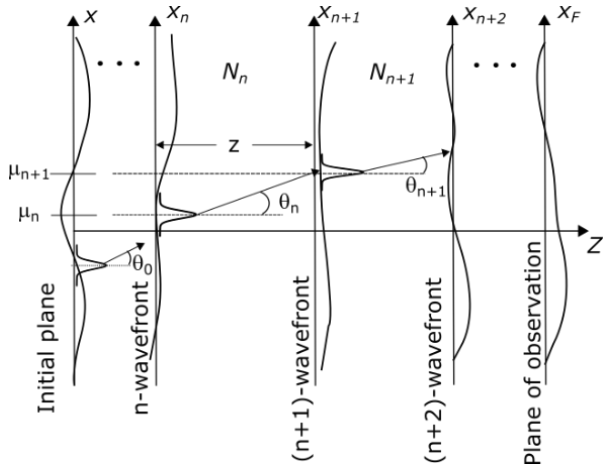

Figure A. 1 Illustration of a Gaussian wavelet propagating from an initial up to an observation plane by iterative propagations, as described in the text.

At the n-wavefront, the analytical equation given by FGSI for the referred wavelet can be written as [24],

$$\Psi_n(x) = A_n \exp(i\alpha_n x)\exp\left(i\beta_n x^2\right)\exp\left(-\frac{(x-\mu_n)^2}{r_n^2}\right)\exp\left(i\gamma_n\left[x-\nu_n\right]^2\right). \quad \text{(A.1)}$$

In Equation (A.1), x_n is replaced by x to allow us to calculate the overall superposition of the wavelet through the optical setup in an iterative manner. The parameter r_n represents the semi-width of the wavelet. At the initial plane, the semi-width of the wavelets is chosen such that the maximum of the wavelet to the left coincides with the $1/e$ value of the wavelet at its right, allowing a uniform distribution of the wavelets at the initial plane. The terms μ_n and ν_n give the spatial and quadratic phase centers of the wavelet respectively. The parameter γ_n gives the value of the quadratic phase and it is set equal to zero at the initial plane. A_n represents the complex amplitude of the wavelet, and corresponds to the complex local amplitude. The parameter α_n allows directing the wavelet (as we describe later). The parameter β_n allows to focus or defocus of the wavelet to represent optical diffracting elements that may be in the optical setup.

As illustrated in Figure A.1, the Gaussian wavelet in Equation (A.1) propagates a distance z , along the optical axis, towards the (n+1)-wavefront. The analytical expression for the propagated wavelet $\Psi_{n+1}(x)$ can be obtained by using the Fresnel diffraction integral [18-19] written as,

$$\Psi_{n+1}(x) = \frac{1}{\sqrt{i\lambda z}} \exp\left(i\frac{2\pi}{\lambda} z \right) \int \Psi_n(s) \exp\left(i\frac{\pi}{\lambda z}(x-s)^2 \right) ds \qquad \text{(A.2)}$$

In Equation (A.2), λ represents the wavelength of the local medium, within the region of propagation. The limits of integration over the parameter s correspond to the region of illumination which, in the case of a Gaussian wavelet, are ± infinity.

After performing the calculations, the propagated wavelet can be written as [24],

$$\Psi_{n+1}(x) = A_{n+1} \exp(i\alpha_{n+1}x) \exp\left(i\beta_{n+1}x^2\right) \exp\left(-\frac{(x-\mu_{n+1})^2}{r_{n+1}^2} \right) \exp\left(i\gamma_{n+1}\left[x-\nu_{n+1}\right]^2\right). \qquad \text{(A.3)}$$

It will be noticed that Equation (A.3) has the same mathematical shape as Equation (A.1), hence the term shape invariant. This characteristic will permit us to calculate the propagation through the optical system in an iterative manner.

As mentioned above, the parameter α_n allows directing the Gaussian wavelet at an angle of propagation θ_n, depicted in Figure A.1. This task is performed by assigning to it the value $\alpha_n = 2\pi N_n / \lambda_0 \tan(\theta_n)$, being N_n the refractive index of the local medium and, λ_0 the free space wavelength.

The analytical expression of the parameters of the propagated wavelet given in Equation (A.3) can be written as [24],

$$\alpha_{n+1} = 0,\ \beta_{n+1} = \frac{\pi}{\lambda z}, \qquad \gamma_{n+1} = -\frac{\pi^2 r_n^4}{D_n \lambda z}\left[(\beta_n + \gamma_n)\lambda z + \pi\right], \qquad r_{n+1} = \frac{\sqrt{D_n}}{\pi r_n}. \qquad \text{(A.4)}$$

In Equation (A.4), for brevity [24],

$$D_n = \lambda^2 z^2 + r_n^4 \left[\left(\beta_n + \gamma_n \right) \lambda z + \pi \right]^2. \tag{A.5}$$

Additionally,

$$\mu_{n+1} = \mu_n + \frac{\alpha_n \lambda z}{2\pi} - \frac{\gamma_n \lambda z \nu_n}{\pi} + \frac{\left(\beta_n + \gamma_n \right) \lambda z \mu_n}{\pi}, \tag{A.6}$$

$$\nu_{n+1} = \frac{\alpha_n \lambda z}{2\pi} - \frac{\gamma_n \lambda z \nu_n}{\pi} - \frac{\lambda^2 z^2 \mu_n}{\left(\pi r_n^4 \right) \left[\left(\beta_n + \gamma_n \right) \lambda z + \pi \right]}, \tag{A.7}$$

$$A_{n+1} = A_n \exp\left(i \frac{2\pi}{\lambda} z \right) \sqrt{\frac{\pi {r_n}^2}{i\lambda z + r_n^2 \left[\left(\beta_n + \gamma_n \right) \lambda z + \pi \right]}} \exp\left(i \gamma_n {\nu_n}^2 \right) \exp\left(i \frac{\lambda z {\mu_n}^2}{r_n^4 \left[\left(\beta_n + \gamma_n \right) \lambda z + \pi \right]} \right)$$

(A.8)

We will use the set of Equations (A.1) - (A.8) to guide each Gaussian wavelet along its path through the propagation process.

As indicated above, at an interface, it may be necessary to change the direction of propagation of the wavelet as we illustrate in Figure A.1 where it can be observed that between the x_n and the x_{n+1} planes and between the x_{n+1} and the x_{n+2} planes, the refractive indexes are equal to N_n and N_{n+1} respectively. The referred wavelet propagates from the x_n -plane towards the x_{n+1} with an angle of propagation θ_n. Then, it propagates with an angle Θ_{n+1} between the x_{n+1} and the x_{n+2} planes, as shown. The relation between the angles follows Snell's law. We will provide the appropriate wavelet angle as follows.

As indicated by Equation (A.4), after each iteration, the next α_n takes a zero value and has to be updated to redirect the wavelet. For this task, first, we have to update the local wavelength, in this case, using the relation $\lambda = \lambda_0 / N_{n+1}$. Here λ_0 is the free-space wavelength. Next, based on Equation (A.6), we use the following relation,

$$\alpha_n = \frac{2\pi}{\lambda}\tan\left(\theta_{n+1}\right) + 2\gamma_n\nu_n - 2\left(\beta_n + \gamma_n\right)\mu_n. \tag{A.9}$$

In Equation (A.9), we have used the fact that, $\tan\left(\theta_{n+1}\right) = \left(\mu_{n+1} - \mu_n\right)/z$, being z the distance between consecutive planes. Finally, to maintain continuity at the interface we must replace the value of A_n by $A_n \exp\left(-i\alpha_n\mu_n\right)$. This process is repeated at each interface to update the direction of the wavelet throughout the overall propagation process.

The parameter β_n allows to focus or defocus of each wavelet due to the presence of optical diffractive components that may be present in the optical setup, as is the case of lenses, as illustrated in detail in [24]. As in this report, we will not include focusing or defocusing components, we will set this parameter equal to zero at the initial plane. We will update this parameter using Equation (A.4) along the propagation process.

Bibliography

[1]. Amiri, M., & Tavassoly, M. T., "Fresnel diffraction from 1D and 2D phase steps in reflection and transmission modes," Optics Communications, 272(2), 349-361. (2007).

[2]. Salvdari, H., Tavassoly, M. T., & Hosseini, S. R., "Fresnel diffraction from a step in the general case," JOSA A, 34(4), 674-680, (2017).

[3]. Tavassoly, M. T., & Salvdari, H., "Fresnel Diffraction from Phase Steps and Its Applications. International Journal of Optics and Photonics," 14(2), 195-208, (2020).

[4]. Tavassoly, M. T., Amiri, M., Darudi, A., Aalipour, R., Saber, A., & Moradi, A. R., "Optical diffractometry," JOSA A, 26(3), 540-547, (2009).

[5]. Tavassoly, M.T., Amiri, M., Karimi, E. and Khalesifard, H.R., "Spectral modification by line singularity in Fresnel diffraction from 1D phase step". Optics Communications, 255(1-3), pp.23-34, (2005).

[6]. Sabatyan, A., & Tavassoly, M. T., "Determination of refractive indices of liquids by Fresnel diffraction," Optics & Laser Technology, 41(7), 892-896, (2009).

[7]. Tavassoly, M. T., Naraghi, R. R., Nahal, A., & Hassani, K., "High precision refractometry based on Fresnel diffraction from phase plates," Optics letters, 37(9), 1493-1495, (2012).

[8]. Tavassoly, M. T., & Saber, A., "Optical refractometry based on Fresnel diffraction from a phase wedge," Optics letters, 35(21), 3679-3681, (2010).

[9]. Tavassoly, M. T., Hosseini, S. R., Fard, A. M., & Naraghi, R. R., "Applications of Fresnel diffraction from the edge of a transparent plate in transmission," Applied Optics, 51(30), 7170-7175, (2012).

[10]. Khorshad, A. A., Hassani, K., & Tavassoly, M. T., "Nanometer displacement measurement using Fresnel diffraction," Applied Optics, 51(21), 5066-5072, (2012).

[11]. Tavassoly, M. T., Haghighi, I. M., & Hassani, K., "Application of Fresnel diffraction from a phase step to the measurement of film thickness," Applied Optics, 48(29), 5497-5501, (2009).

[12]. Hassani, K., Ashrafganjoie, M., & Tavassoly, M. T., "Application of white light Fresnel diffractometry to film thickness measurement," Applied optics, 55(7), 1803-1807, (2016).

[13]. Motazedifard, A., Dehbod, S., & Salehpour, A., "Measurement of thickness of thin film by fitting to the intensity profile of Fresnel diffraction from a nanophase step," JOSA A, 35(12), 2010-2019, (2018).

[14]. Dashtdar, M., & Hosseini-Saber, S. M. A. “Focal length measurement based on Fresnel diffraction from a phase plate,” Applied Optics, 55(26), 7434-7437, (2016).

[15]. Ghoorchi-Beygi, M., & Dashtdar, M., “Single-shot measurements by Fresnel diffraction of divergent waves from a phase plate,” Applied Optics, 59(7), 1968-1973, (2020).

[16]. Mahmoudi, A., “Application of Fresnel diffraction to fabrication and characterization of glass phase steps,” Applied Optics, 57(16), 4558-4562, (2018).

[17]. Mahmoudi, A., “Application of Fresnel diffraction from phase steps to measurement of etching rate of transparent materials,” Applied Optics, 54(26), 7993-7996, (2015).

[18]. Hassani, K., Jabbari, A. and Tavassoly, M.T., “Application of Fresnel diffraction from a phase step to determination of the spectral line profile”. Journal of Optics, 20(9), p.095606, (2018).

[19]. Aalipour, R., Tavassoly, M. T., & Saber, A., “Measuring source width and transverse coherence length using Fresnel diffraction from a phase step,” Applied Optics, 59(25), 7712-7719, (2020).

[20]. Aalipour, R., & Aminjafari, M., “Phase shift calibration based on Fresnel diffraction from phase plates,” Journal of Optics, 14(12), 125706, (2012).

[21]. Siavashani, M. J., Naghedi, I., Abbasian, V., Akhlaghi, E. A., Charsooghi, M. A., Tavassoly, M. T., & Moradi, A. R., “3D imaging using scanning diffractometry,” Scientific Reports, 11(1), 1-10, (2021).

[22]. Salvdari, H., & Tavassoly, M. T., “Fresnel diffraction from the edge of a transparent plate in the general case,” JOSA A, 35(3), 496-503, (2018).

[23]. Sheveleva, A. and Finot, C., “Temporal Fresnel diffraction induced by phase jumps in linear and nonlinear optical fibers,” Results in Physics, 19, p.103344, (2020).

[24]. Onural, L., “Sampling of the diffraction field. Applied Optics,” 39(32), 5929-5935, (2000).

[25]. Mas, D., Garcia, J., Ferreira, C., Bernardo, L. M., & Marinho, F. “Fast algorithms for free-space diffraction patterns calculation,” Optics communications, 164(4-6), 233-245, (1999).

[26]. Falaggis, K., Kozacki, T., & Kujawinska, M., “Computation of highly off-axis diffracted fields using the band-limited angular spectrum method with suppressed Gibbs related artifacts,” Applied Optics, 52(14), 3288-3297, (2013).

[27]. Freniere, E. R., Gregory, G. G., & Hassler, R. A., “Edge diffraction in Monte Carlo ray tracing. In Optical design and analysis software,” (Vol. 3780, pp. 151-157), SPIE, (1999, September).

[28]. M. Cywiak, A. Morales, J.M. Flores, M. Servín, “Fresnel-Gaussian shape invariant for optical ray tracing,” Opt. Express 17 (13) 10564–10572, (2009).

[29]. M. Cywiak, M. Servín, A. Morales, “Diffractive and geometric optical systems characterization with the Fresnel Gaussian shape invariant,” Opt. Express 19 (3), 1892–1904, (2011).

[30]. Cywiak, M., Cywiak, D., & Yáñez, E., “Finite Gaussian wavelet superposition and Fresnel diffraction integral for calculating the propagation of truncated, non-diffracting and accelerating beams”. Optics Communications, 405, 132-142, (2017).

[31]. J. W. Goodman, “Introduction to Fourier Optics,” (Roberts and Company Publishers, 2005), pp. 66-67.

[32]. K. Iizuka, Engineering Optics, (Springer Verlag, 1986). pp. 68-71.

[33]. Anaya-Vera, S., & Cordero-Davila, A., “Fast and exact diffraction integral calculus: A comparison with Fresnel approximation,” Optik, 208, 164470, (2020).

[34]. Bahmanpour, S., & Mahmoudi, A. “Application of Fresnel diffraction from the edge of a transparent plate to measurement of glucose concentration,” Applied Optics, 60(10), 2893-2897, (2021).

[35]. Yáñez, E., Cywiak, M., & Cywiak, D., “Gaussian beam with high spherical aberration focused by a singlet lens-shaped container for glucose measurements,” Applied Optics, 58(31), 8495-8500, (2019).

[36]. Luis M. González, Moisés Cywiak, and David Cywiak, “Theoretical and experimental study of optical diffractometry based on Fresnel diffraction from a transmission phase step”, Applied Optics, 62(25), 6593-6602, (2023).

[37]. Meyrath, T. P., Schreck, F., Hanssen, J. L., Chuu, C. S., & Raizen, M. G., “A high frequency optical trap for atoms using Hermite-Gaussian beams,” Optics Express, 13(8), 2843-2851, (2005).

[38]. Lebedev, N. N., “Special functions and their applications. Dover Publications,” INC. pp 136-139, (1972).

[39]. Cywiak, M., & Cywiak, D., “Multi-Platform Graphics Programming with Kivy,” Apress. pp. 173-190, (2021).

[40]. G.A. Siviloglou, et al., Observation of accelerating airy beams, Phys. Rev. Lett. 99 (21) (2007) 213901.

[41]. D. Choi, et al., Generation of finite power airy beams via initial field modulation, Optics Express 21 (16) (2013) 18797–18804.